universität wien

MASTERARBEIT / MASTER'S THESIS

Titel der Masterarbeit / Title of the Master's Thesis

„High cycle fatigue investigations of a biodegradable Mg5Zn-alloy processed by severe plastic deformation“

verfasst von / submitted by

Moritz Hartleb, BSc

angestrebter akademischer Grad / in partial fulfilment of the requirements for the degree of

Master of Science (MSc)

Wien, 2020 / Vienna, 2020

Studienkennzahl lt. Studienblatt / degree programme code as it appears on the student record sheet:	UA 066 876
Studienrichtung lt. Studienblatt / degree programme as it appears on the student record sheet:	Masterstudium Physik
Betreut von / Supervisor:	Ao. Univ.-Prof. Mag. Dr. Erhard Schafler

Acknowledgements

I would like to thank my supervisor *Prof. Erhard Schafler* for giving me the opportunity to work on this topic as well as his continuous help, valuable comments and useful critique for this thesis. Furthermore I would like to express special thanks to *Prof. Michael Zehetbauer* for giving me the opportunity to work on his project 'Topologically Designed Mg-Alloys for Biomedical Applications' and to go to the 29th Colloquium on Fatigue Mechanisms in Brno, Czech Republik. Great thanks are also due to *Dr. Andrea Ojdanic* for laying the groundwork for the tests I performed in this work by providing all the needed data on the Mg5Zn alloy as well as instructing me on all machines used for sample preparation.

Furthermore I would like to thank the team of the Insitute of Chemical Technologies and Analytics from TU Vienna: *Prof. Golta Khatibi* for allowing me to use her groups ultrasonic testing device, for the invaluable help with fatigue experiments, and fracture analysis, *Mag. Thomas Walter* for his help with electron microscopy, *Dr. Bernhard Czerny* for performing the vibrometry measurements, *Dr. Martin Lederer* for his FEM simulations and *Vinayak Chavan MSc.* for accoustic measurements.

Additionally I want to express my gratitudes towards *Martina Hofmann* from the Faculty Center for Nanostructure Research for help with optical microscopy and *Iris Wonsch* from the faculty's machine shop for her technical support and swift realistations of the tools designed for this work.

Finally, I wish to thank my parents Karin and Helmut Hartleb, my brother Clemens Hartleb and my partner Anna Razumovsky for their tireless support and without whom I would not have been able to come this far.

Abstract

Using biocompatible metallic materials for surgical implants allows the use of samples that gradually degrade in vivo and then, after healing of the target area completely dissolve. The advantages include the prevention of a second surgery, increased tissue healing due to dissolved materials and the low Young's modulus of the implant material comparable to that of bone, thus reducing stress shielding. In this regard magnesium and its alloys show great promise, yet they need to be specially designed to withstand the imposed external stresses and to circumvent the brittle nature of Mg.
This work focuses on the fatigue behaviour of a potential Mg-alloy, Mg5Zn (wt.%) in five different conditions:

1. thermal dissolution of precipitates
2. deformed at room temperature
3. deformed at room temperature with additional heat treatment
4. deformed at elevated temperatures (285℃)
5. deformed at elevated temperatures with additional heat treatment

The fatigue behaviour is an important aspect in designing implants, as they need to keep their structural integrity long enough for complete healing of the target tissue.
Samples were deformed using high pressure torsion (HPT) to induce grain refinement and increase mechanical properties without significant changes in the Young's modulus. HPT deformation at room temperature with additional heat treatment introduced vacancy agglomerates that impede dislocation movement substituting additional alloying elements, while HPT deformation at elevated temperatures introduces precipitates into the hexagonal matrix which also hinder dislocation movement.
Fatigue tests were performed at a frequency of 20kHz, with complete reversal of strain, up to 1e9 cycles at ambient conditions. Due to sample size limitations of HPT deformation a special set-up was used in the fatigue tests, where samples with an hourglass geometry were glued onto a sample holder attached to an acoustic horn. To fully quantify the effect of the sample geometry and special set-up, finite element analysis and laser doppler vibrometry measurements were performed.
To achieve the aforementioned sample geometry, samples were punched using spark erosion machining to prevent changes in the microstructure which would occur with

conventional machining methods. Multiple tools were designed and improved upon to yield a satisfying result and electro- and mechanical polishing were both compared in their usefulness to produce smooth sample faces.
The ultrasonic fatigue tests revealed an increase in fatigue strength in all four conditions when compared to the non deformed material. However, samples deformed at elevated temperatures with and without heat treatment did not increase the fatigue resistance as much as samples deformed at room temperature. Fracture surfaces show a ductile behaviour for all samples except the samples deformed at room temperature with additional heat treatment, where a more brittle morphology can be observed. Furthermore the crack paths of the different conditions were analysed using light microscopy, which revealed that all samples, even that deformed at room temperature exhibited a more serrated crack path along one of its two faces.

Kurzfassung

Die Verwendung von biokompatiblen metallischen Materialien im Rahmen von chirurgischen Implantaten erlaubt es diesen in vivo zu korrodieren und, nachdem der betroffene Bereich geheilt ist, sich komplett zu zersetzen. Vorteile dieser Methode sind, dass es keiner weiteren Operation bedarf um das Implantat wieder zu entfernen, als auch, dass die aufgelösten Stoffe aktiv zum Heilungsprozess beitragen können. Biokompatible Materialien die hier zum Einsatz kommen müssen des Weiteren einen E-Modul sehr nahe an dem von Knochen haben um „stress shielding“ vorzubeugen.
Magnesium eignet sich für solche Anwendungen, wenn man seine Sprödheit und geringe Härte umgehen kann. Dazu wird es vor der Anwendung durch legieren und spezielle mechanische und/oder thermische Behandlung manipuliert, um äußeren Spannungen standzuhalten.
In dieser Arbeit werden die Ermüdungseigenschaften einer solchen Mg-Legierung, Mg5Zn (wt. %), in fünf verschiedenen Zuständen untersucht:

1. thermische Auflösung von Ausscheidungen
2. Verformung bei Raumtemperatur
3. Verformung bei Raumtemperatur mit anschließender Wärmebehandlung
4. Verformung bei einer Temperatur von 285°C
5. Verformung bei einer Temperatur von 285°C mit anschließender Wärmebehandlung

Ermüdungsverhalten ist ein wichtiger Aspekt bei der Entwicklung von Implantaten, da die strukturellen Eigenschaften mindestens bis zur Heilung des betroffenen Bereichs bestehen müssen.
Proben wurden mittels Hochdrucktorsion (HPT) verformt um Kornfeinung zu erzeugen als auch um mechanische Eigenschaften zu verbessern ohne den E-Modul des Materials signifikant zu verändern. HPT Verformung bei Raumtemperatur erzeugt Leerstellenagglomerate, welche die Bewegung von Versetzungen behindern und so als Ersatz für weitere Legierungsatome dienen sollen. HPT Verformung bei hoher Temperatur erzeugt intermetallische Ausscheidungen in der hexagonalen Matrix welche ebenfalls die Versetzungsbewegung einschränken sollen. Ermüdungsversuche wurden bei einer Frequenz von 20kHz, mit komplett reversiertem Zug-Druck, auf bis zu 1e9 Zyklen unter Laborbedingungen durchgeführt. Um den Limitationen in der Probengröße durch die Verformung

mittels HPT gerecht zu werden wurde ein spezielles Setup verwendet, bei dem eine Probe mit einer „hourglass“-Geometrie auf einen Probenhalter geklebt wurde. Um die Auswirkungen dieses Aufbaus genau zu analysieren wurden finite Elemente Messungen und Laser-Doppler-Vibrometer Messungen durchgeführt.
Die „hourglass“-Geometrie der Proben wurde mittels Funkenerodierens erreicht, um eine Veränderung der Mikrostruktur zu verhindern. Im Rahmen der Probenvorbereitung wurden mehrere Stanzwerkzeuge entwickelt und im Lauf der Arbeit verbessert um zufriedenstellende Resultate zu erzielen. Ebenfalls wurde sowohl elektrisches- als auch mechanisches Polieren hinsichtlich der Rauheit der finalen Probenoberfläche verglichen.
Die Ermüdungsversuche ergaben, dass sich die Behandlung der Proben positiv auf ihre Ermüdungseigenschaften ausgewirkt hat. Proben die bei hohen Temperaturen behandelt wurden, mit und ohne Wärmebehandlung, haben jedoch einen weitaus geringeren Anstieg an Ermüdungsresistenz gegenüber Proben die bei Raumtemperatur verformt wurden. Die Bruchflächen zeigen ein zähes Verhalten, außer bei Proben verformt bei Raumtemperatur mit anschließender Wärmebehandlung wo ein spröder Bruch zu erkennen ist. Zudem wurden Rissverläufe der Proben mittels eines Lichtmikroskops analysiert welche zeigen, dass selbst Proben die bei Raumtemperatur mittels HPT deformiert wurden, zumindest auf der Seite welche näher zum Ort der Rissentstehung liegt, einen nicht geraden Rissverlauf aufweisen.

Contents

1 Theoretical background

1.1 Defects in crystals

Defects in crystals are categorized by their dimension including 0D (vacancies or interstitial atoms), 1D (dislocations), 2D (grain boundaries) and 3D (stacking faults) and are present in every real crystal.

1.1.1 Point defects

Point Defects are 0D defects thus including only the removal of single atoms or small clusters of atoms (in the case of agglomerates) from their positions in an ideal crystal. These atoms can either move to the surface and leave behind a vacancy or move to an interstitial location, creating a Frenkel-pair [1][2]. Point defects can be created by either quenching, irradiation with electrons or neutrons or plastic deformation and are inherently included in any material as they are introduced during solidification from the melt. Eq. 1 furthermore shows that there are vacancies present at any finite temperature.

$$c_v \propto exp(-H_v^f/k_BT) \tag{1}$$

where c_v is the total concentration of vacancies, H_v^f the vacancy creation enthalpy, k_B the Boltzmann constant and T the temperature in Kelvin [3].
For each temperature there is also a chance that not only single vacancies form, but also vacancy agglomerates of two or more (di- tri- ect. vacancies). These can be energetically favourable as their creation enthalpy is $H_{2V}^f = 2H_V^f - H_b$. H_b is the binding enthalpy which is the difference between adding the first vacancy and then adding a second one next to it. The concentration of di- to mono- vacancies can be correlated as shown in eq. 2.

$$n_{2v} \propto exp(H_b/k_BT) \cdot {n_v}^2 \tag{2}$$

Thus at lower temperatures the concentration of divacancies is higher than at high temperatures, were monovacancies dominate. At different cooling rates and sample geometries different vacancy defect compositions can be achieved [2],[4].

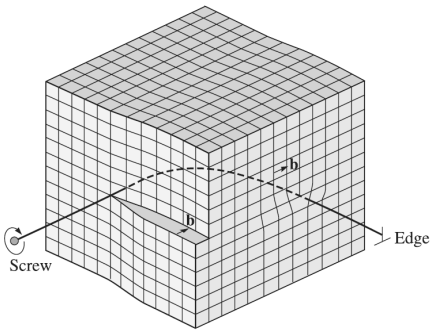

Figure 1: A mixed dislocation changing its type in a crystal, screw dislocation at the front and edge dislocation at the side [3].

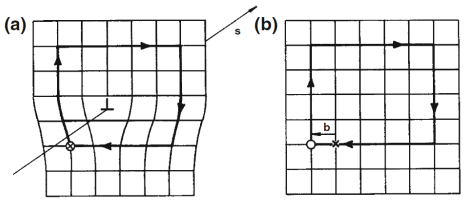

Figure 2: Schematic construction of the Burgers vector associated with an edge dislocation [5].

1.1.2 Dislocations

Dislocations are 1D defects which allow the crystal to plastically deform. They can be visualized by cutting the crystal along a plane and then moving the two parts of the crystal either perpendicular or parallel to the edge of the cut, which is called the dislocation line. A perpendicular displacement gives rise to an edge dislocation, while parallel displacement causes screw dislocations as seen in fig. 1 [2], [1]. If the dislocation line is curved the displacements direction relative to it changes and so does the character of the dislocation, giving rise to mixed types [3]. The amount of displacement caused by a dislocation is given by its burgers vector **b**. It is constructed by first following the lattice clockwise (according to the right hand rule) around the disturbed area and then repeating the process in the undisturbed lattice. **b** is the vector required to close the loop in the undisturbed lattice from its final position to the start (compare fig. 2) [3]. A dislocation that leaves the lattice causes the crystal to be sheared by $\gamma = b/l$, where l is the crystal thickness [1].

1.1.3 Grain Boundaries and Twin Boundaries

Grains are areas in the crystal where the arrangement of the lattice is identical. If two grains of different orientation meet a grain boundary will be produced at their interface. If the misorientation is small the grain boundary can be constructed by dislocations (so called small angle grain boundaries) while at larger angles this is no longer possible, giving rise to high angle grain boundaries [3]. Twin boundaries are special forms of grain boundaries, where the two grains are mirror images of each other. This mechanism is especially prevalent in hexagonal materials as it offers an additional way for the material to plastically deform [6].

1.2 Strengthening

Mechanical strength is a materials ability to withstand plastic deformation or failure when external forces are applied. As plastic deformation is carried by the movement of dislocations through the crystal, reducing their mobility is the key to increasing the materials strength [7]. An increase in strength can be caused by the Hall-Petch relation, the Taylor equation [8] and precipitation hardening [1] which will be described in the following chapters.

1.2.1 Hall-Petch relation

In polycrystalline materials the random orientation of grains and their grain boundaries gives rise to an increase in external stress required to cause plastic deformation. There are multiple important factors to be considered when plastically deforming a polycrystalline material. Firstly, due to the random orientation not all grains will start to deform plastically at the same time, as some are oriented more convenient to the external force than others. Additionally the atomic misfit caused by grain boundaries including twin boundaries [9] prohibits the movement of dislocations from one grain to the next, causing pile ups at the edges. These pile ups cause stress in the neighbouring grains, where they induce dislocations. Lastly deformed grains need to keep contact to their neighbouring grains, else the crystal falls apart [7]. Experimentally all these factors can be summarized in the Hall-Petch equation

$$\sigma_y = \sigma_0 + K_{HP} \cdot d^{-1/2} \tag{3}$$

where σ_y is the yield stress, d the grain size and K_{HP} and σ_0 material constants. With severe plastic deformation methods additional hardening factors are introduced such as

the formation of nanoclusters, nanotwins and dislocation substructures which can lead to increases in strength of up to a factor $3-8$ [8] which exceeds the values predicted solely by Hall-Petch.

1.2.2 Taylor equation

As dislocation density is increased during plastic deformation, their mean free path is reduced resulting in strain hardening. This is caused by the interaction of the moving dislocation with, either parallel or orthogonal dislocations (so called forest dislocations) in its vicinity [1]. These two processes are described by the Taylor equation

$$\tau = \tau_0 + \alpha \cdot G \cdot b \cdot \sqrt{\rho} \tag{4}$$

where τ_0 is the flow stress necessary to overcome obstacles other than those from dislocation interactions, G is the shear modulus, b is the Burgers vector, ρ represents the density of dislocations and α the strength of the interaction [10].

1.2.3 Precipitation hardening

Similar to defects such as vacancies and dislocations, precipitates act as a barrier for dislocation movement through the crystal. There are two ways for dislocations to interact with such precipitates, the Kelly-Fine and the Orowan mechanism, depending on the precipitate size. The Kelly-Fine mechanism, active at small radii, describes the movement of dislocations through the precipitate, which is called cutting. On the other hand the Orowan mechanism describes the bowing out of dislocations to encapsulate the precipitates and pass them this way [11]. The method that is energetically favourable is chosen which depends strongly on the size of the precipitate and the force required to overcome it. Fig. 3 shows the change of the active mechanism with increasing precipitate size. Eq. 5 quantifies the Orowan mechanism which is dominant for precipitation hardening in this work.

$$\tau = \frac{G \cdot b}{l - 2r} \tag{5}$$

Here G is the shear modulus, b is the burgers vector, l is the mean distance of the precipitates and $2r$ the precipitate diameter. It emphasizes the importance of the volume fraction of the precipitates as an important factor in the mean free path of dislocations [1].

There will be a closer look on different shaped precipitates in hexagonal materials in

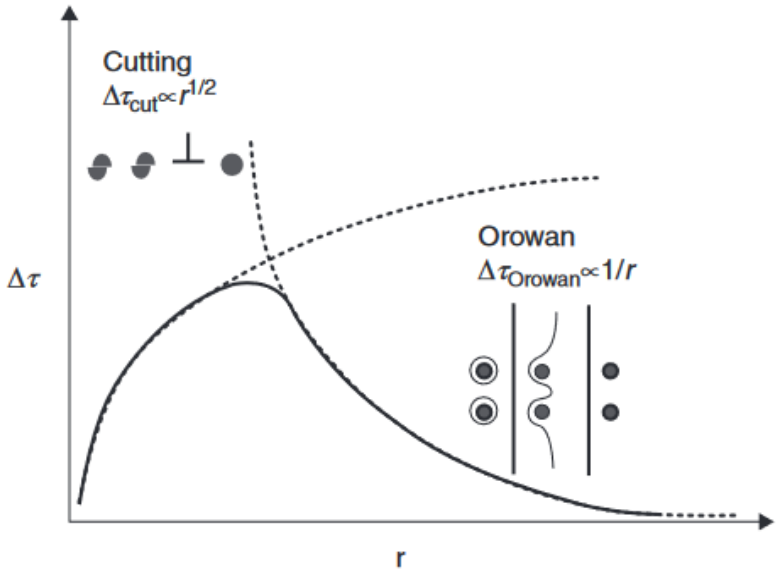

Figure 3: Effect of precipitate size on the strengthening caused by cutting and Orowan mechanism [11].

chapter 1.3.2. Depending on their shape, these have a varying influence on hardening as their effective spacing in the lattice is different at the same number density. This can be seen in fig. 4 where prismatic platelets contribute the most to hardening, while basal platelets contribute the least at all number densities.

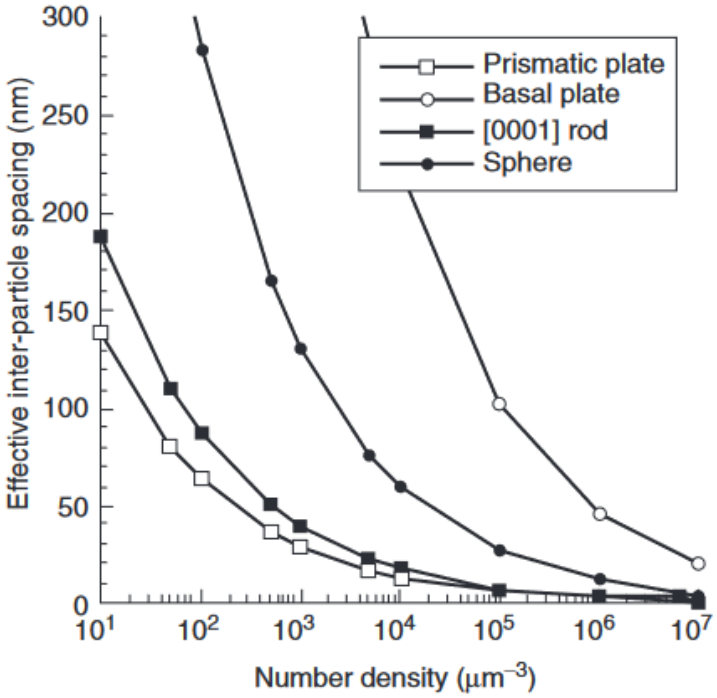

Figure 4: Effective inter-particle spacing l of precipitates with varying geometry depending on their density considering same aspect ratio and volume fraction [11].

1.2.4 Vacancy-agglomerates

When ageing Mg isochronally and isothermally there is a distinct strength peak at 170°C that was first observed by Hampshire and Hardie in [12]. This is due to the movement of vacancies at higher temperatures, which allows them to form agglomerates. In hexagonal materials this happens preferably in the close packed basal plane [13]. As these are the preferred slip planes, the effect is significant in hcp materials [2]. If the agglomerates surpass a certain threshold size, they collapse forming dislocation loops as seen in fig. 5, which are only stable until certain temperatures where the dislocations in the loop tend to evaporate [12]. As these loops act as pinning points, dislocations can only overcome these dislocation loops by means of Orowan mechanism [2]. The strengthening is given by the Kirchner formula

$$\Delta\tau = \frac{G \cdot b}{k} \cdot N^a \cdot d^{3a-1} \tag{6}$$

where G is the shear modulus, b the burgers vector, N the density of the loops and d the average loop diameter, k and a are constants depending on the ratio of loop distance to their diameter [13]. In anisotropic lattices, $k = 0.122$ and $a = 1/2$ holds true [2].

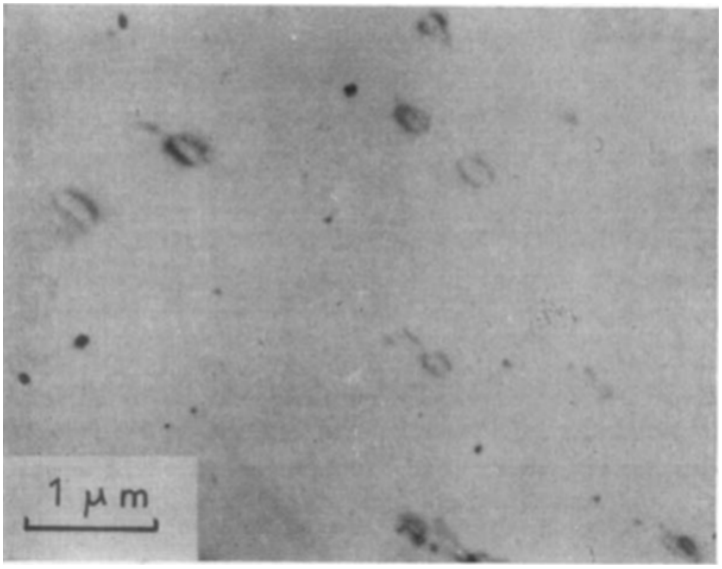

Figure 5: Dislocation loops in quenched and aged Mg [12].

1.2.5 Severe plastic deformation

A powerful tool to introduce defects that contribute to strengthening is severe plastic deformation (SPD). It is a top-down technique to introduce nano crystalline grains into materials. Grain sizes smaller than 500nm [14] can be produced by plastic deformation with true strains bigger than 1000% [15]. The most common methods for SPD are high pressure torsion (HPT) and equal channel angular pressing (ECAP). Both of which have advantages over other SPD methods as they provide a uniform distribution of nanostructures in the material while preventing cracks and other forms of mechanical damage during deformation [15].

1.2.6 High pressure torsion (HPT)

Torsion experiments have always been useful to determine the stress-strain behaviour at larger strains where tensile testing fails, due to necking. By introducing a high hydrostatic pressure during the deformation, fracturing can be prevented entirely. The resulting strain for a disc-shaped sample in an ideal HPT experiment is given by

$$\gamma = \frac{2 \cdot \pi \cdot n}{t} \cdot r \tag{7}$$

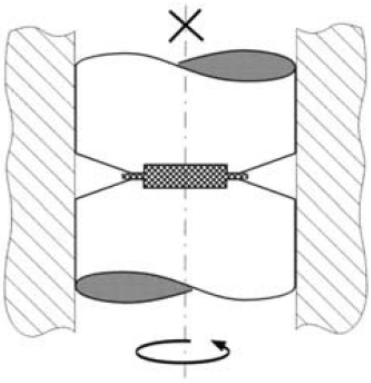

Figure 6: Schematic HPT set-up [4].

which can be converted to von Misses equivalent strain

$$\varepsilon = \frac{2 \cdot \pi \cdot n}{t \cdot \sqrt{3}} \cdot r \tag{8}$$

where n is the number of revolutions, t is the thickness of the sample and r is the distance from the rotation axis [4].

This shows that strain can be applied continuously in contrast to other SPD methods and although Eq. 7 and eq. 8 show that strain is dependant on the distance from the center this can be circumvented by going to high values for n thus reaching saturation values for the strain for all relevant radii.

The experimental set-up is given in f ig. 6. Prior to inserting the sample the top and bottom anvils are sandblasted to provide good friction between them and the sample to prevent slipping. The sample is then placed between the two anvils with a cavity slightly smaller than the initial height of the disc. The applied pressure is typically set between $1 - 10$GPa depending on the material that is processed causing a small amount of the metal to flow out of the cavity. In this ring zone the pressure applied on the material prohibits any further flow of the material outwards which in return induces a hydrostatic pressure in the processing zone. Another benefit to the flow of the material is that the anvils do not touch, which could lead to their failure [4]. If necessary the anvils can be heated or cooled externally to control the deformation temperature [4].

Despite its many benefits HPT has the disadvantage of producing only disc-shaped samples with diameters up to $20mm$ and thickness of $1mm$ [14] limiting their usefulness in industrial applications.

1.3 Properties of hexagonal closed packed (hcp) materials

In an ideal hcp structure atomic planes are arranged in the sequence ABABAB... describing the alternation of two equivalent planes as depicted in fig. 7 where the atoms are represented by hard spheres. In this representation it is useful to define the atomic packing factor (APF) describing the volume occupied by atoms relative to the volume of the unit cell. Hcp structured materials have an $APF = 74.048$ which is the highest possible [5]. This is achieved by having a relation of the width of the base a to the hight of the unit cell c of exactly $c/a = 1.633$ [5]. In such systems the close-packed plane is the

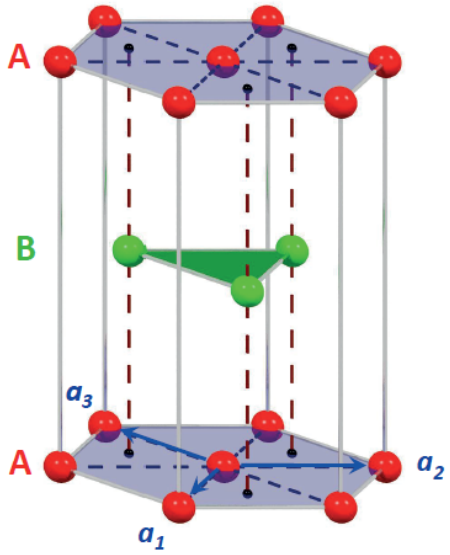

Figure 7: Hcp structure showing the ABABAB... arrangement [5].

(0001) basal plane with close-packed directions $\langle 11\bar{2}0 \rangle$ and the shortest lattice vectors being $\frac{1}{3}\langle 11\bar{2}0 \rangle$. This is the slip system that is most often observed [7] while other such as prismatic slip and pyramidal slip [16] need a higher resolved shear stress to be activated, which greatly influences the strength and ductility.

1.3.1 Slip mechanisms and twinning

For plastic deformation of materials near grain boundaries von Mises showed that at least 5 independent slip systems are needed [17]. Slip is favoured in close packed planes and directions, which for Mg systems is (0001) and $\langle 11\bar{2}0 \rangle$ respectively [7]. A list of available slip systems and their direction is given in table 1 and schematically represented in fig. 8, where slip direction describes which basis vectors are involved in the deformation. Stresses to activate slip in different planes and directions can differ greatly as described

in [11] for Mg single crystals where the basal slip has a critical resolved shear stress (CRSS) of 5MPa, prismatic slip has a CRSS of 20MPa and pyramidal slip has a CRSS of 40MPa.

Because of the high CRSS needed in hcp materials to allow plastic flow in the c direction, twinning occurs. During twinning, atoms arrange to form a mirror plane to the initial crystal, which causes a predefined amount of shear stress [18]. Fig. 9 shows possible twinning planes in Mg.

Slip system	**Slip direction**	**Slip plane and direction**	**Independent slip systems**
Basal	a	$\{0001\}\ \langle 11\bar{2}0\rangle$	2
Prismatic	a	$\{10\bar{1}0\}\ \langle 11\bar{2}0\rangle$	2
Pyramidal type I	a	$\{10\bar{1}1\}\ \langle 11\bar{2}0\rangle$	4
Pyramidal type II	a+c	$\{11\bar{2}2\}\ \langle 11\bar{2}3\rangle$	5

Table 1: possible slip systems in Mg after [19].

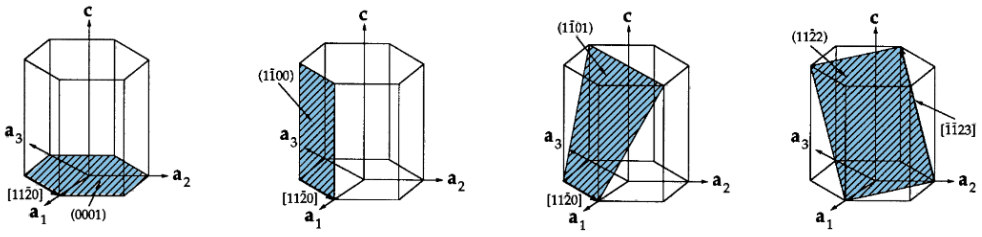

Figure 8: Possible slip systems for Mg, from left to right: basal, prismatic, pyramidal type I and pyramidal type II slip.

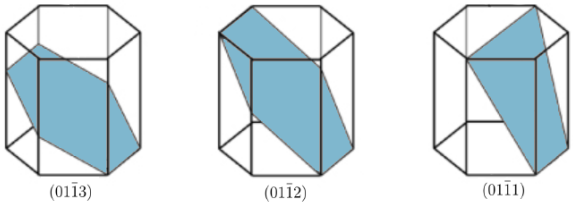

Figure 9: Possible twinning planes in Mg.

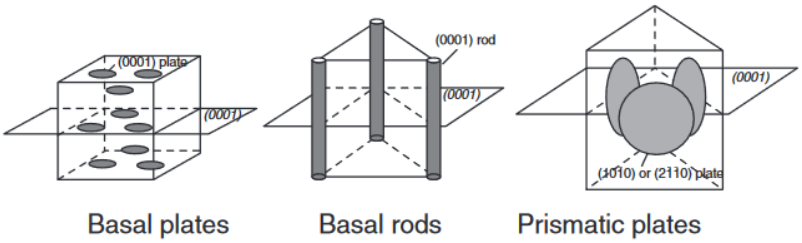

Figure 10: Schematic view of the types of precipitates in Mg [11].

1.3.2 Precipitates in HCP materials

Precipitates are a second phase within the supersaturated solid solution. To form these precipitates the net free energy change ΔG has to be considered. It is a superposition of the free energy change due to the interface of the precipitate and the matrix, the energy associated with the volume of the precipitate and the increase due to a lattice misfit [11]. Although precipitation initially increases the free energy, after a threshold radius r^* is reached, there will be spontaneous growth until a critical size is reached, depending on the temperature. Such events usually occur at sites which reduce the free energy term corresponding to the interface and the stress such as defects of any dimensionality.
While the above is based on spherical precipitates, depending on the interface between the precipitate and the matrix, growth in a certain direction might be favoured. In Mg this results in 3 different types of precipitates: basal platelets, basal rods and prismatic plates as seen in fig. 10 when atleast one alloying element is present [11].

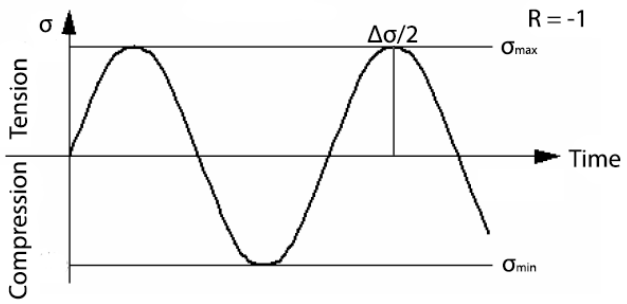

Figure 11: Schematic tension and compression cycles.

1.4 Fatigue

Fatigue research has its roots in the 19^{th} century when railway accidents occurred due to cyclic failure of axles [20]. This led to the first systematic research by Wöhler and has since been an important topic in all load bearing applications ranging from airplane components to biomedical implants and consumer products.
In fatigue the applied stresses are often very small and below the yield stress, yet because of its many repetitions failure can occur [3].
Important parameters to consider when talking about stress controlled cyclic fatigue, independent if the stress is axial, torsional or flexural [20], are as follows (see fig.11) :

- stress amplitude $\Delta\sigma/2 = (\sigma_{max} - \sigma_{min})/2$
- number of cycles to failure N_f (which is sometimes written as $2N_f$ if the number maxima and minima of loading are both taken into consideration)
- load ratio $R = \sigma_{min}/\sigma_{max}$
- stress intensity factor range ΔK

Depending on N_f one either speaks of low cycle fatigue (LCF) with $N_f \leq 1e5$ cycles, high cycle fatigue (HCF) which ranges from $1e6$ to $1e7$ cycles and ultra high cycle fatigue (UHCF) which is also called giga cycle fatigue for cycles until failure of $1e8$ to $1e11$ cycles with different mechanisms being dominant in each regime (see. chapter 1.4.1) [21].
Most common fatigue testing machines operate at $0.01 - 10$Hz. Testing e.g. $1e7$ cycles at this frequency would take at least 12 days, any measurements in the UHCF regime would be practically impossible. Thus ultrasonic resonance machines have been developed in order to perform tests at 20kHz severely reducing the time needed for a single measurement [20].

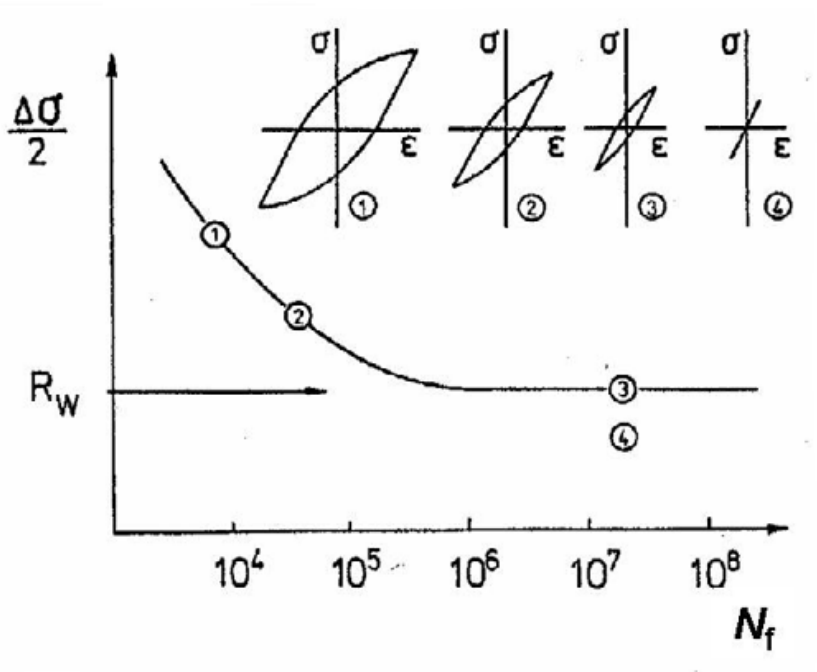

Figure 12: Schematic Wöhler curve with corresponding hysteresis loops [22].

1.4.1 Fatigue life representations

Fatigue life is usually represented by the Wöhler or S-N diagram, compare fig. 12 where the stress amplitude is plotted against the number of cycles to failure. Additionally a plateau (R_W) is indicated in the HCF regime where the fatigue lifetime should become infinite [22]. The inset in fig. 12 shows how a single cycle looks in a conventional stress-strain diagram at the corrsponding points. To no surprise smaller strains result in higher fatigue life (compare the points 1 - 3 in fig. 12), yet only at point 4 a purely elastic behaviour can be seen [23].
The plot in fig. 12 is a composite of the Coffin-Manson law

$$\frac{\Delta\varepsilon_{pl}}{2} = \varepsilon'_f(2N_f)^c \tag{9}$$

for the LCF regime, where $\frac{\Delta\varepsilon_{pl}}{2}$, ε'_f and c denote the plastic strain amplitude, the fatigue ductility coefficient and the fatigue ductility exponents respectively, as well as the Basquin relation

$$\frac{\Delta\varepsilon_{el}}{2} = \frac{\sigma'_f}{E}(2N_f)^b \tag{10}$$

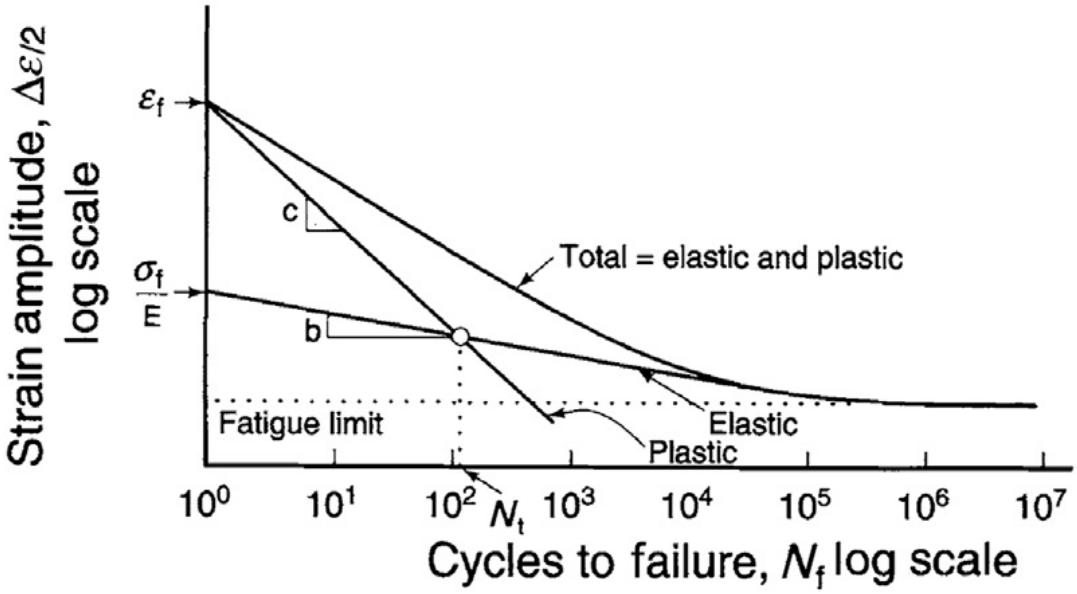

Figure 13: Transition from low to high strain fatigue by change of the dominant mechanism [24].

for the HCF regime where $\frac{\Delta\varepsilon_{el}}{2}$, σ'_f and b denote the elastic strain amplitude, the fatigue strength coefficient and the fatigue strength exponents respectively [22].
Adding eq. 10 and eq. 9 and plotting logarithmically one can define N_t which denotes the transition from low to high strain fatigue as seen in fig. 13 [24].

1.4.2 Stress intensity factor and Notch effect ΔK

Notches, pores, micro-cracks or other small flaws in a material increase the local stress. In simple cases under uniaxial stress, e.g. tensile testing, the relation is governed by

$$K = f\sigma\sqrt{\pi a} \tag{11}$$

where a is the size of the flaw, f is a geometry factor and K is the stress intensity factor. As soon as K reaches a ctritical value K_c (by either increasing the applied stress σ or the flaw-size a) the flaw is allowed to grow [3].
Under cyclic deformation the size of cracks is not constant but changes and can even reach zero (full crack closure), depending on the load ratio R, thus changing the crack propagation ratio [20]. Therefore one uses $\Delta K = K_{max} - K_{min}$ to describe cyclic processes.
If notches of controlled geometry are introduced into a sample the stress at these sites

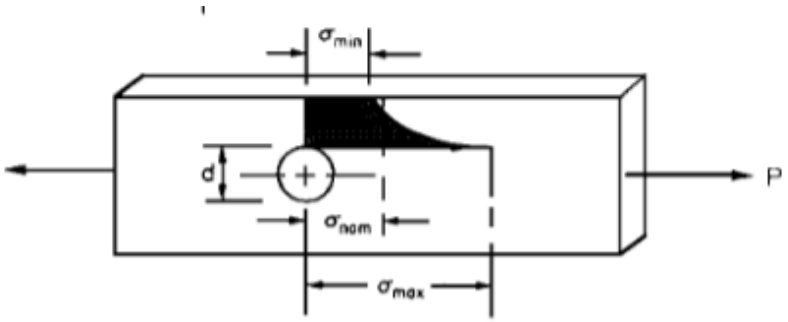

Figure 14: Changes in the stress on a sample dependent on the distance from a circular hole of diameter d [27].

is increased, compare fig. 14, this change in stress is described by the theoretical stress concentration factor

$$K_t = \frac{\sigma_{max}}{\sigma_{nom}} \tag{12}$$

where σ_{max} is the maximum stress at the notch site and σ_{nom} is the stress in the same sample, without the notch [25]. Values for K_t are widely available in literature for a multitude of different notch and sample shapes (compare e.g. [26]). In fatigue testing K_t is often replaced by the fatigue notch factor K_f which describes the relative change in fatigue lifetime when notches are introduced compared to a smooth surface as described by eq. 13.

$$K_f = \frac{S_{Nunnotched}}{S_{Nnotched}} \tag{13}$$

Although similar in principle, $K_f \leq K_t$ holds true in most cases and only approaches the theoretical value for large notch radii and high strength materials [27].

1.4.3 Fatigue life mechanisms

Depending on the applied stresses, fatigue is categorized into multiple regimes. Fig.15 shows these regimes as the S-N plot is divided into four categories:

I LCF regime governed by Manson-Coffin law described in Eq. 9. Cracks initiate at the surface.

II Surface cracking due to persistent slip band (PSB) creation.

III Crack-initiation at internal inhomogeneities.

IV No irreversible internal damage is produced, no internal nor external cracks are initiated [21].

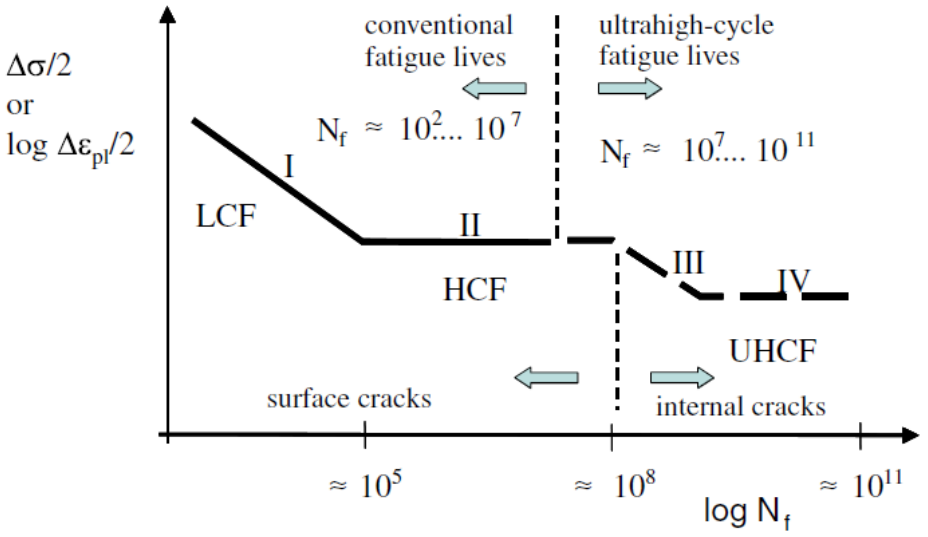

Figure 15: Fatigue life stages depending on applied stress or strain[28].

As this work focuses heavily on stage II the effects that occur during fatigue testing will be discussed in further detail.
On the microscopic level the process during fatigue can be separated into three domains as shown in fig. 16 [20].

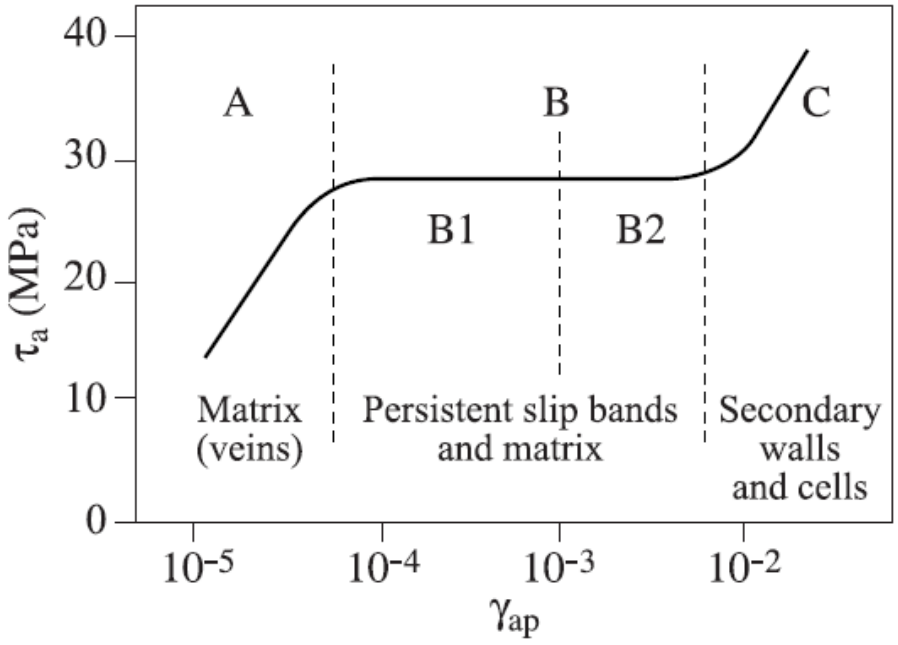

Figure 16: 3 domains in the process of single crystal deformation [20].

In regime A, although the yield stress is not exceeded, there are some dislocations in conveniently oriented grains, which are able to move [29]. If dislocations of opposite sign that move this way meet each other while below a threshold distance, they get trapped and form a dislocation dipole. This is only possible for edge dislocations as screw dislocations could cross slip to annihilate [27]. Electron microscopy confirms, that after a short time these dislocations form what is called the vein structure, where dislocation rich areas are seperated by dislocation poor areas as seen in fig. 17. This causes rapid hardening in the sample as can be seen in the increase in shear stress τ_a in fig. 16.

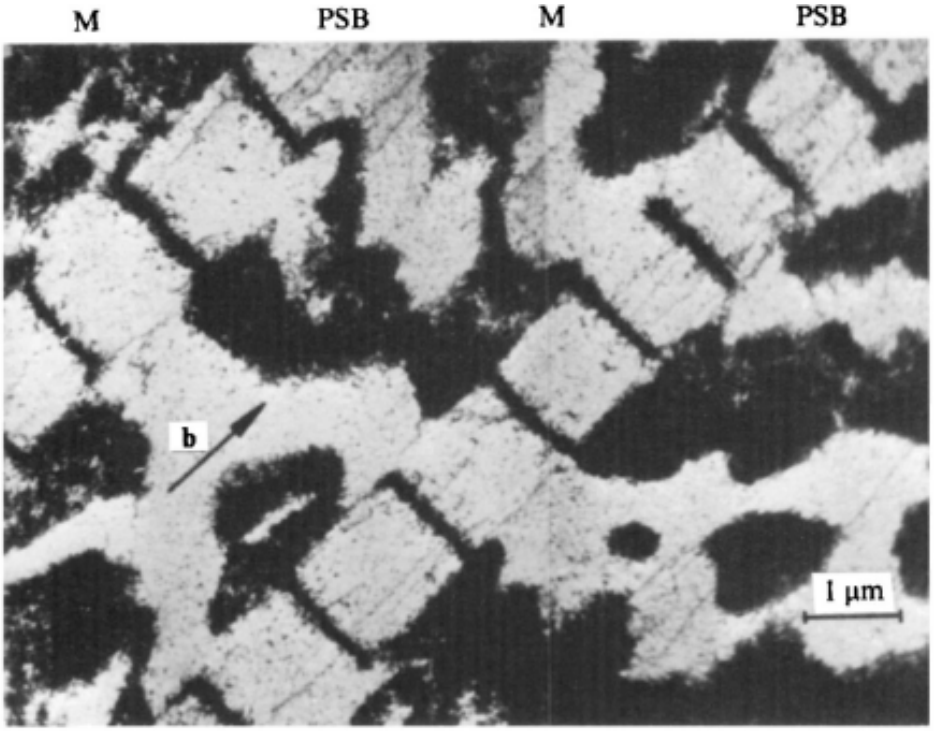

Figure 17: Vein structure and ladder structure seen in a fcc single crystal [27].

Once the vein structure has been established any further increase in shear strain γ_{ap} causes the creation of PSBs [20] to accommodate further increases in strain [27]. PSBs are softer areas surrounded by a harder matrix [27] [30], thus they carry the plastic deformation. The rapid creation of vacancies and dislocations in them create a net volume increase on the material, causing a roughening of the surface by intrusions and extrusions, as seen in fig. 18. This is described in regime B, where over the course of cycling the PSB concentration increases. PSB creation is initiated within the dislocation veins, where there are small areas of low dislocation density. Those areas are surrounded by a

harder dislocation rich shell. With a constant movement of these shells a ladder structure is formed from the dislocation veins. With continued cycling during this phase, the volume fraction f of the PSBs increases up to 100% to accommodate further strain. PSBs are the sites of the first micro cracks, where intrusions and extrusion cause an increase in stress. If further strained, secondary slip systems are activated which transform the PSBs into a cell like structure (regime C). The secondary crack formation begins usually at an obstacle like a grain boundary or a precipitate. The speed at which the crack propagates follows the Paris power law [20]

$$\frac{da}{dN} = C(\Delta K)^m \tag{14}$$

where a is the crack length, N is the number of cycles, ΔK is the change in the stress intensity factor (see chapter 1.4.2), m is the Paris power factor which is $2 - 6$ in most materials [20] and C a material constant. Depending on ΔK there are 3 regimes for crack propagation speed.

- Area A where $\Delta K \leq \Delta K_T$ (the threshold stress concentration factor) the crack does not further propagate
- Area B where Paris law (eq. 14) holds.
- Area C where $\Delta K \geq \Delta K_C$ where catastrophic failure occurs nearly instantly

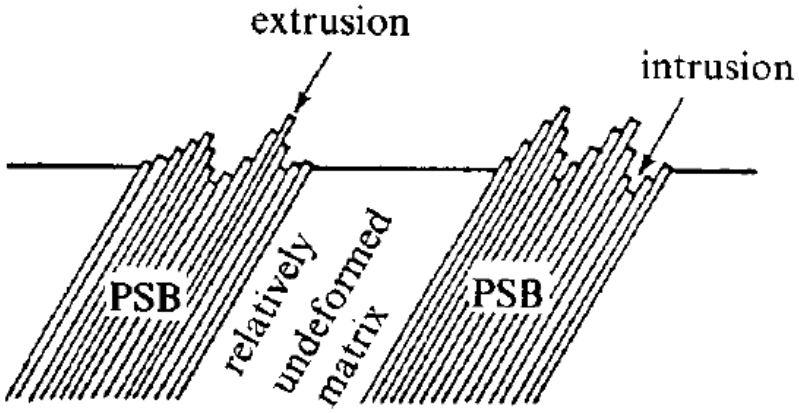

Figure 18: effects of slip on the material surface [27].

In polycrystalline materials, the same effects occur as in single crystals but interactions with precipitates and grain boundaries may change the behaviour drastically. PSBs can form either on the surface grains or in bulk grains, while the first can leave the crystal

to relieve stress, the latter are confined by neighbouring grains, and the dislocations pile up at the grain boundaries [30].

1.4.4 Fatigue in hexagonal systems

In hexagonal single crystals the anisotropy of the lattice is of importance as different orientations lead to different behaviour during testing. The most important difference to other crystalline structures is the tendency of hcp materials to create cyclic twins [31] regardless of their grain orientations (see [31]). Twins contribute to increased hardening as they impede dislocation movement and cause grain refinement (compare to chapter 1.3.1). As hcp materials do not necessarily have access to multiple slip systems the orientation of the grains may also suppress the creation of the typical cell structure if only single slip and cross slip are available. Then only the dislocation dipole structure is observed [31].

2 Experimental techniques

2.1 Investigated Materials

In a previous study done by Ojdanic (see [32]) various Mg alloys were tested for their use as biomedical implants. Mg with 5wt% Zn, abbreviated as Mg5Zn, showed the best results of those tested and was thus further investigated on its fatigue properties in this study. Zn is an essential trace element in the human body and thus is non toxic. The alloy containing $3wt\%$ Zn shows the best ductility but has poor strength while at 5wt% Zn there is a good trade-off between the two [11].
The material was provided by the Austrian institute of Technology. The provided Mg5Zn was tested for its chemical composition showing that an average of 5.25 ± 0.03wt% Zn was contained in the alloy [32].
Scanning electron microscopy (SEM) images of the as-cast alloy can be seen in fig. 19, where bright spots indicate the pressence of a $Zn_{13}Mg_{12}$ precipitate with a composition of 75.86 ± 3.9 at% Mg and 24.14 ± 3.4 at% Zn.
These precipitates were dissolved by either thermal treatment at 350℃or a combination of thermal and mechanical treatment at 285℃, which will be abbreviated as *IS* and *HPT@285℃* respectively from now on. Both methods result in a supersaturated solid solution with a different degree of remaining precipitates. Furthermore one batch of the *IS* samples, where precipitates were dissolved thermally, was then HPT deformed

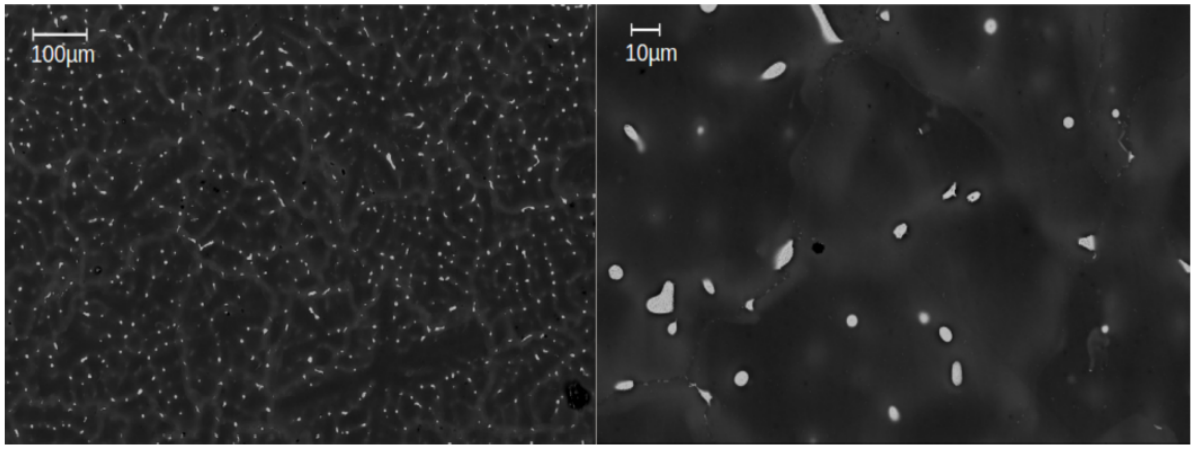

Figure 19: SEM image of primary precipitates in Mg5Zn [32].

at room temperature, abbreviated as *HPT@RT*. Furthermore one set of both types of HPT deformed samples was then isothermally heat treated, denoted as *HPT@RT+HT* and *HPT@285℃+HT* from now on.
Samples of type *IS* were used as a baseline to allow a comparison between the increases in fatigue properties caused by the different preparation methods.

2.2 Sample preparation

2.2.1 Cutting

The provided rods were cut into 10*mm* thick discs at the faculty's workshop, as seen in fig. 20. Further cutting was done by a Charmilles Eleroda 110 EDM Electrical Discharge Machine. An electric potential is placed between the sample and an electrode, in the case of cutting a thin brass wire. The whole set-up is suspended in petroleum, a dielectric liquid, causing a rapid creation of sparks between the two charged surfaces, which melt the target material without mechanical contact. The wire has a thickness of 0.2mm and can be rotated at different speeds to ensure the continuous creation of sparks. Additionally further capacitors can be activated to increase the size of the sparks, which speeds up the cutting process by increasing the spark size. This however causes a rougher surface and a bigger loss of material. There is a continuous flow of petroleum in the cutting chamber to flush away any debris which would otherwise block further eroding of the sample.
The discs described above were initially cut into 10mm $\times$ 10mm rods as seen on the right side of fig. 20. For this a hose was used for a more localized flushing of the cut, as the

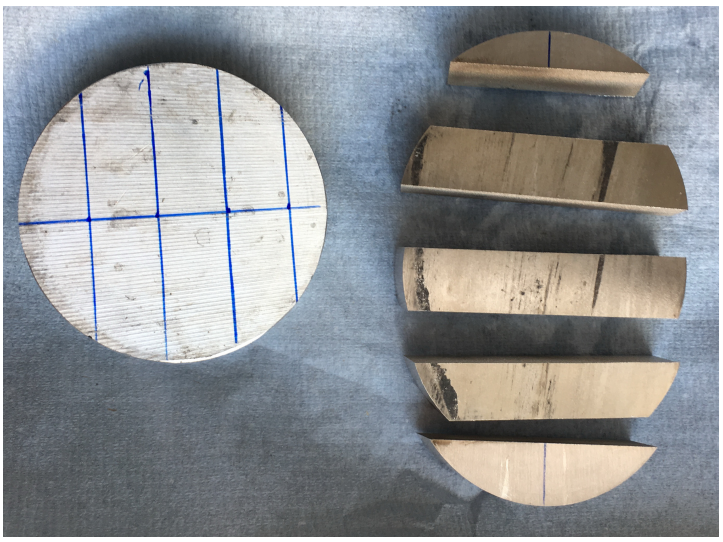

Figure 20: Initial material before being cut on the left hand, after being cut by EDM on the right hand.

brass wire is prone to failing if there is too much debris at the cutting surface.
Rods were then turned into cylinders of 10mm radius in the faculty workshop to be further cut into small discs that were fit to be deformed by HPT. The EDM was set to cut discs of thickness 1.3mm with an additional capacitor with a capacity of 2μF turned on. Some of the resulting discs can be seen in fig. 21 which had a thickness of approximately 0.9mm.
For all the following steps these initial discs were used as the basic raw material to be further manipulated and were the basis for two samples which were in the end cut using the EDM with the thin brass wire as described above. This prevents the fragile disc from bending and from the introduction of defects into the material.

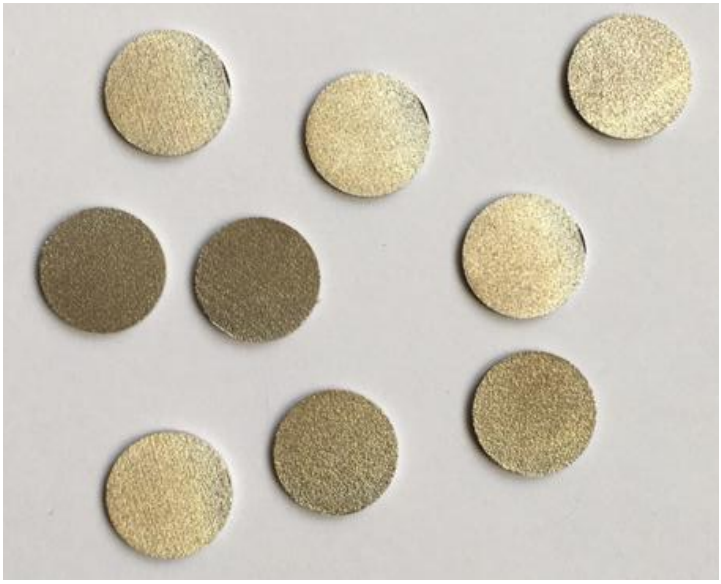

Figure 21: Small discs after cutting by EDM.

2.2.2 Homogenization of *HPT@RT* and *HPT@RT+HT* samples

For thermal dissolution of primary precipitates previously cut discs were briefly ground with a $P600$ sandpaper to remove any possible contamination caused by cutting with the brass wire, as Cu atoms could diffuse into the material at elevated temperatures. These Cu atoms not only hinder the creation of the super saturated solid solution but are also toxic when used in implants. This resulted in discs with a final thickness of about $0.8mm$. Samples were then placed carefully into the central part of the furnace to ensure that all samples were exposed to the same set temperature. As Mg is prone to oxidation, homogenization in the furnace was conducted in an Ag atmosphere. To ensure that no oxygen was left in the chamber, it was flushed with Ag and then evacuated. This process was repeated four times. Finally the furnace was set to a temperature of 350°C for 25h, where 1h was needed to reach the desired temperature. After the set time the samples were furnace cooled by switching the furnace off and letting them rest for at least 30 minutes. The removed samples were oxidised slightly on their surface, which was removed by grinding the discs briefly with a $P1200$ polishing paper. Fig. 22, taken from [32] shows a SEM image of Mg5Zn after homogenization which when compared to fig. 19 shows a significant decrease of primary precipitates due to this treatment.

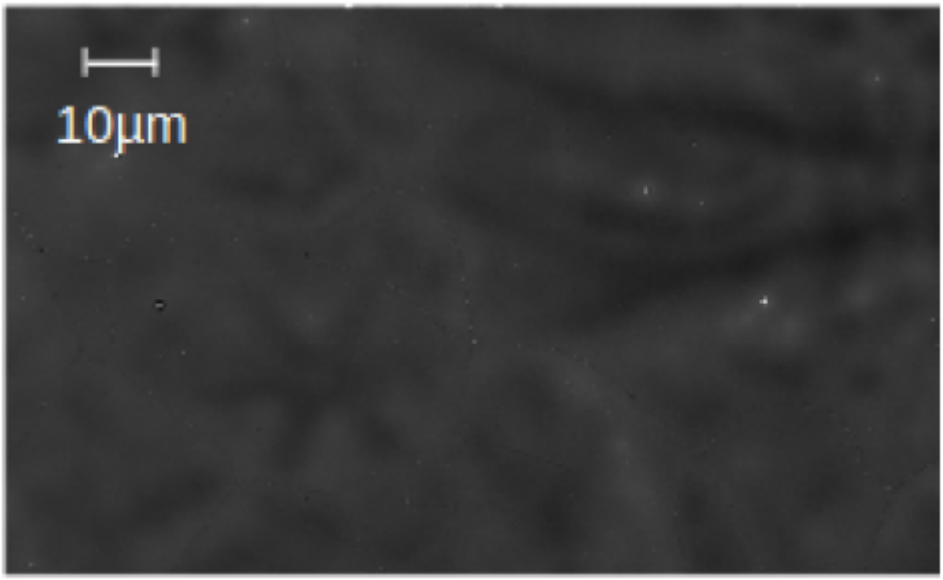

Figure 22: Mg5Zn after thermal dissolution of precipitates. White spots indicate a higher concentration of Zn (compare fig. 19)[32].

2.2.3 High pressure torsion at room temperature

After homogenization in the furnace samples were deformed by means of HPT at room temperature to achieve a nanocrystalline structure. The machine can be seen in fig. 23. For this deformation, samples were placed in between two anvils with a total depth of $t = 0.6$mm and a radius of $r = 5$mm. The applied pressure was 4GPa. The anvils were sandblasted prior to HPT testing to provide sufficient friction, so that the discs were subjected to the entire deformation of $n = 0.5$ rotations, at a set speed of 0.2rpm, and did not slip. To ensure that samples do not slip, they were marked with lines on the front and back. As one half of the sample is moved against the other, one of the markings rotates by 180°. Using eq. 8 and the given values, the resulting equivalent strain is $\varepsilon = 15.12$ at the edge of the sample. The HPT process refines grains to a size of about $50 - 400$ nm [32], while also introducing dislocations and vacancies into the material. In [32] Ojdanic calculated the values using differential scanning calorimetry resulting in a vacancy concentration $c_v = 1 * 10^{-3} \pm 1 * 10^{-4}$ and a dislocation density $c_d = 3 * 10^{-4} \pm 1 * 10^{-4}$.

Figure 23: HPT used to deform samples.

2.2.4 High pressure torsion at elevated temperature

HPT deformation at high temperature was used to combine mechanical and thermal dissolution of primary precipitates. Using the same pressure of 4GPa aswell as samples of the same diameter of 10mm the samples were deformed at 10 revolutions with a rotation speed of 0.3rpm. For this deformation the sample was placed into the anvils and a load was applied. Then the anvils were inductively heated to 285℃. As the surface temperature of the anvils was measured the actual deformation was started after a minimum of 1min of heating to ensure that the core of the anvils was at the desired temperature as well. After the HPT process the inductive heating and the applied pressure were turned off and the samples were left to cool to room temperature. Ojdanic measured an increase in vickers hardness of around 35% for Mg5Zn with no radial dependency and noted that this was the best way to achieve the super saturated solid solution state [32]. As with the previous chapter Ojdanic calculated the vacancy and dislocation concentration for HPT deformation at 285℃ as well, with the vacancy concentration being $c_v = 7 * 10^{-4} \pm 1 * 10^{-4}$ and the dislocation density $c_d = 2 * 10^{-5} \pm 6 * 10^{-6}$

2.2.5 Ageing by isothermal heat treatment

Samples of category *HPT@RT+HT* and *HPT@285℃+HT*, as described in chapter 2.1 were subjected to ageing, where samples are heated in a silicon oil bath at 100℃ for $24h$. After this, samples were quenched in water to freeze the microstructure that was created during this process [32].

2.2.6 Properties after processing

This chapter will provide a short overview of the material properties for each of the 5 conditions, that are important for fatigue testing. Data is taken from [32] and [13] and shown in table 2. The grain size for *IS* was measured by means of the intercept method, where a line is drawn across a sample and the number of times it crosses a grain boundary is recorded. The grain size is given by the ratio of the length to the number of grain boundaries that were crossed. For all samples the poisson's ratio was taken as $\nu = 0.343$, which is relevant for finite element analysis. For sample type *HPT@285℃* and *HPT@285℃+HT* grain sizes of 10-40μm were obeserved. In between grains big precipitates in the order of 100nm are visible. Additionally prismatic platelets, 5-20nm long and less than 1nm thick as well as basal platelets were present.

Condition	E [GPa]	UTS [MPa]	σ_{yield} [MPa]	d	elongation [%]
IS	44 ± 4	174 ± 57	90 ± 10	450 μm	20
HPT@RT	50 ± 4	303 ± 20	280 ± 10	$50 - 400$ nm	5
HPT@RT+HT	46 ± 2	329 ± 36	310 ± 26	$50 - 400$ nm	5
HPT@285℃	34 ± 1	215 ± 5	155 ± 20	$10 - 40$ μm	19
HPT@285℃+HT	34 ± 1	245 ± 40	160 ± 10	$10 - 40$ μm	19

Table 2: Average values for Young's Modulus (E), ultimate tensile strength (UTS), yield stress (σ_{yield}) and grain size (d) and elongation until failure during tensile testing as well as their standard deviation for the Mg5Zn conditions used in this work.

2.2.7 Punching and final sample shape

To achieve the desired sample geometry as shown in fig. 24 samples were punched by the same EDM machine as described in chapter 2.2.1 were this time a punching head was used as the electrode. The desired thickness of the sample was 0.2mm and the width of the samples at its thinnest was 0.35mm. Samples were fixed in a sample holder as seen in fig. 25. The two different types of designs for the lids are shown in fig. 26. While having three holes to guide the punching cylinders (fig. 26 a) separately allows for a repeatable and precise placement of the holes, which is significant for HPT samples, as deformation is dependant on the distance from the center, the drawback is, that if the holes and the heads are not perfectly aligned they get tilted slightly when moving downwards, causing a trapezoidal crosssection of the sample. If the punching cylinders are not guided by individual holes (fig. 26 b) they are more likely to be parallel but it is harder to center the punching head over the sample. To fix this issue small markings were put on the sample and sample holder to align the sample.
Also different approaches for punching heads were chosen to study their effectiveness in achieving the small dimensions of the sample. Here too, it is most important to ensure that the punching head and the sample are perpendicular to each other. The punching head was carefully screwed into the EDM by stepwise tightening of the screws that fixate it. Furthermore to avoid vibrations that could move the sample holder, the basin in which the punching took place was screwed tight.

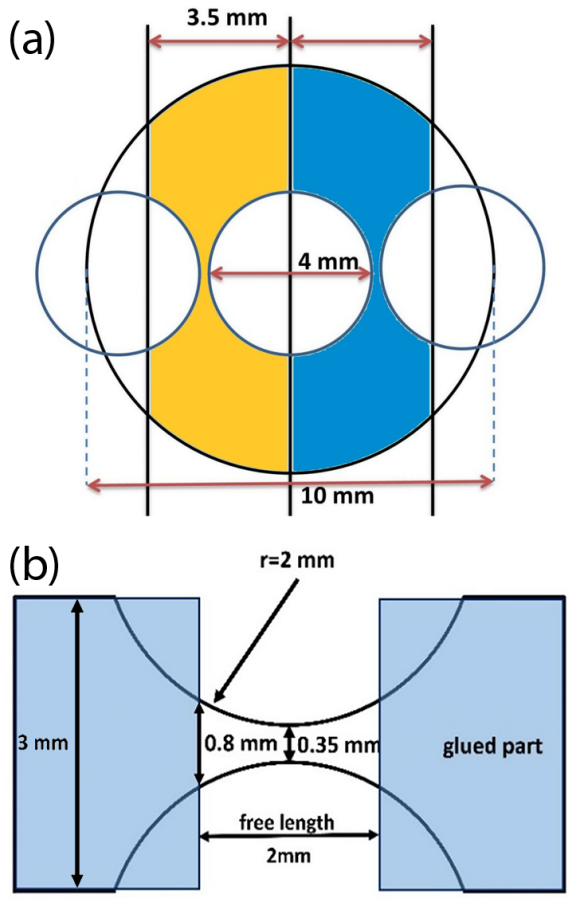

Figure 24: Schematic of sample dimensions after punching is shown in (a). The yellow and blue area show the two samples that are obtained from the final cut. (b) shows a the sample ideal sample dimensions [33].

The first punching head design used can be seen in fig. 27. Even though the cylinders were chosen to be short to avoid vibration during punching, the inclusion of threads caused the two halves of the sample to be asymmetrical causing a difference up to 15% so that their experimental behaviour differed significantly. Additionally the punching heads were slightly angled resulting in trapezoidal shape of samples.
The second punching head was designed without any threads. For this *Schneidestempel DIN 9861 D HSS* were used as seen in fig. 28. A negative of the angled head was machined into the holder to keep the punching rods straight and in place . Yet due to machining limitations, even though the samples now had a square crosssection, the distance between the three rods still led to a constant difference of 7% between the two samples punched from a disc. This punching head can be seen in fig. 29 (a).
In the last set-up only the center rod was used and the whole head was moved to punch

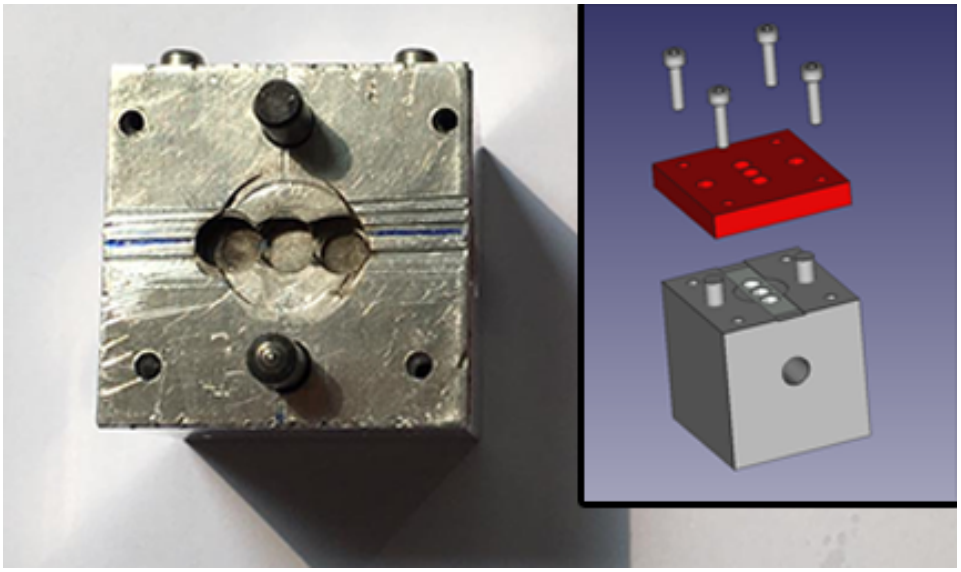

Figure 25: Sample holder used during punching. The right image shows the original design.

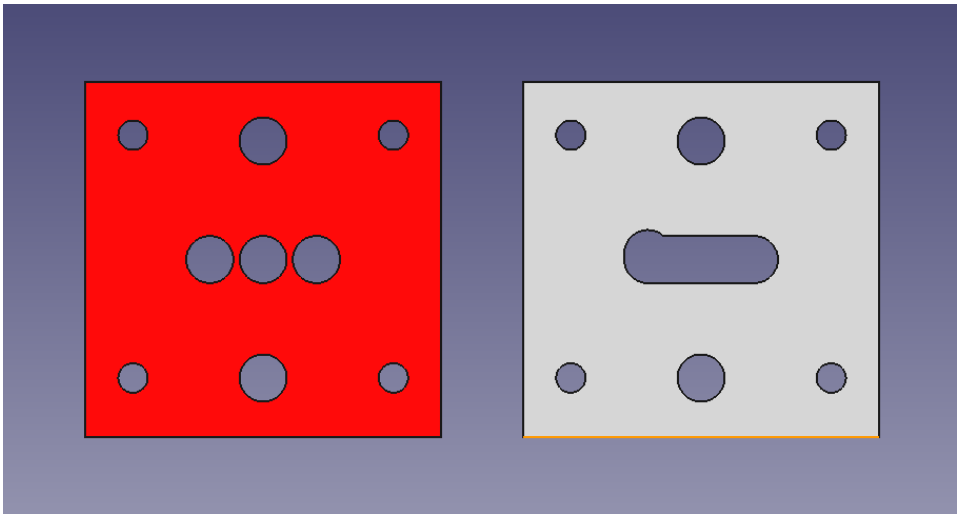

Figure 26: The two types of covers used to fixate the samples during punching. On the left, each punching head is guided individually. On the right, a zero position is set using a notch and the punching head is moved from left to right, to punch the holes one after the other.

the three holes individually. To achieve a good placement of the holes a notch was put into the lid to keep the initial position of the cylinder the same for all samples. This set-up is shown in fig. 29 (b) and the corresponding lid on the right side of fig. 26. Fig. 30 shows both set-ups with the thread-less punching head schematically.

Samples of type *HPT@285℃* were prepared using 3 cylinders, not guided by individual

Figure 27: Initial punching tool used for sample preparation. Due to the punching heads being fastened via threads the sample geometry was non uniform and comparable fatigue results could not be achieved.

Figure 28: *Schneidestempel DIN 9861 D HSS* was inserted in the punching head, the conical head forces it to stay in place during sample preparation without the use of threads.

holes. All other samples were prepared using only the central cylinder to punch the individual holes.

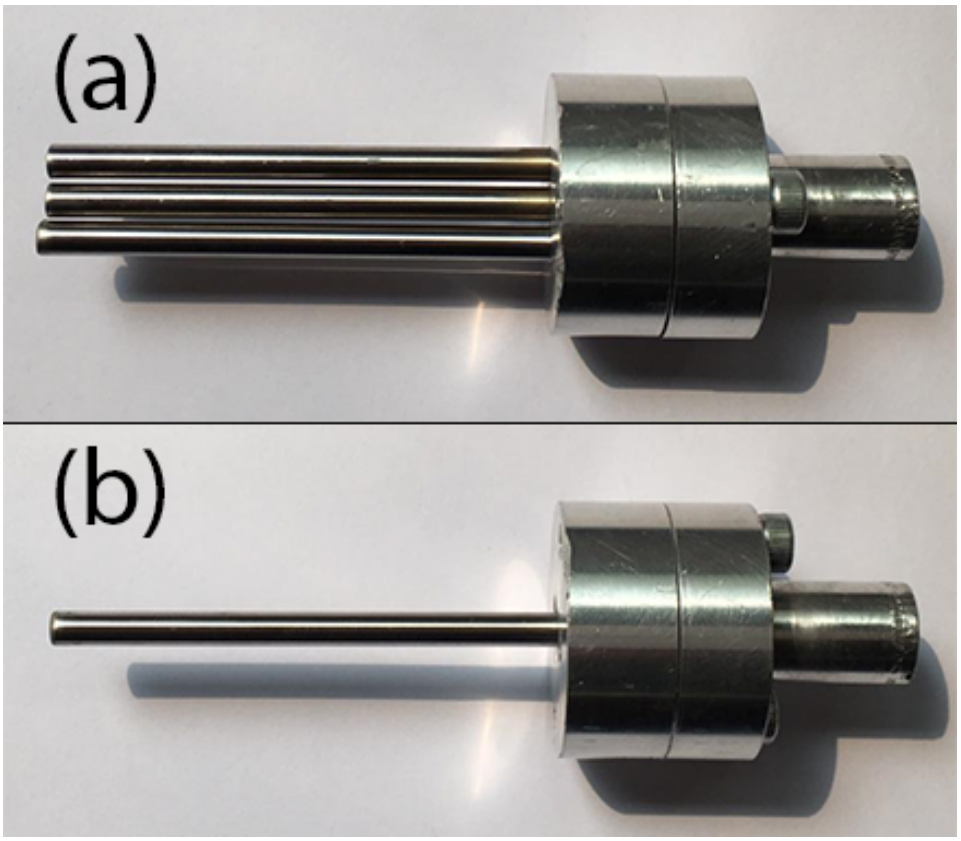

Figure 29: Tool used to punch the samples.

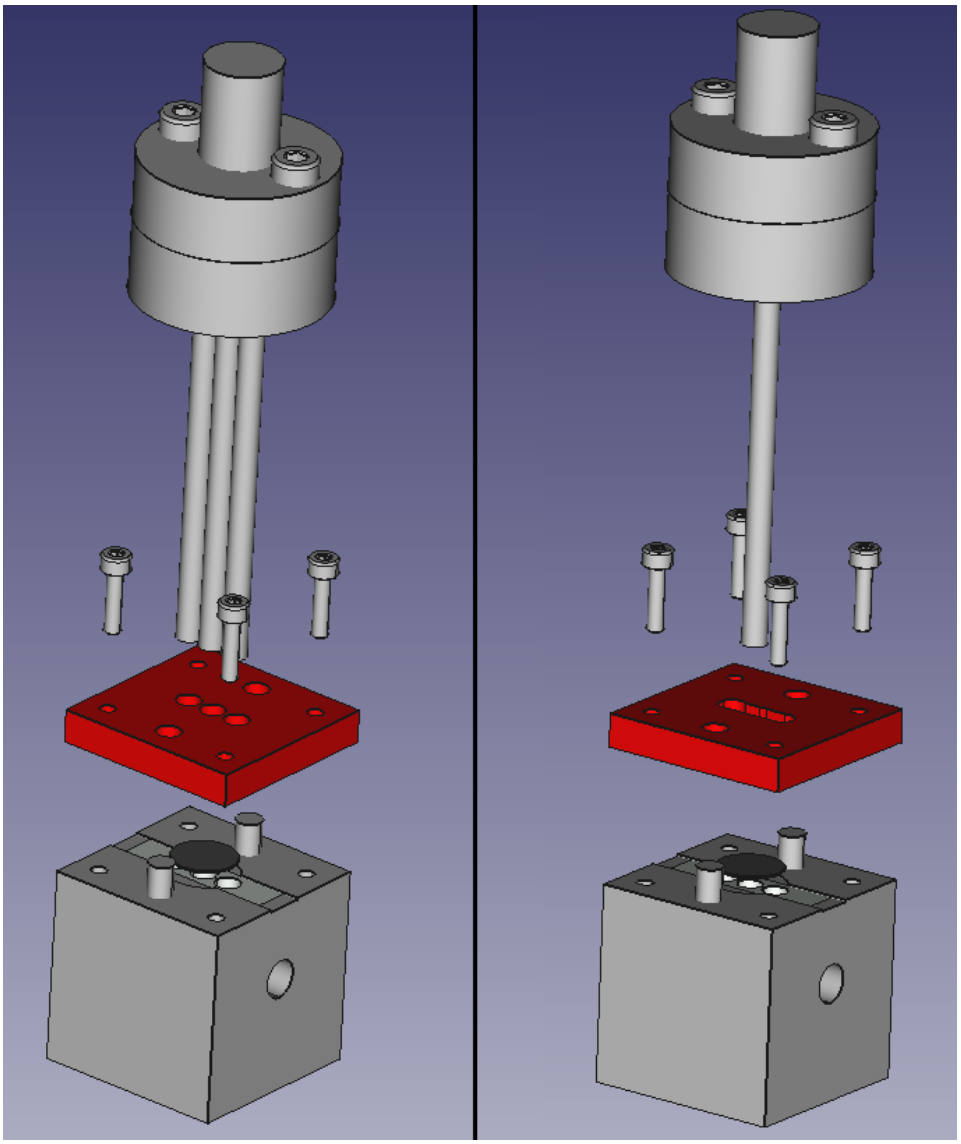

Figure 30: View of the punching tool with 3 punching heads shown in (a) and with one punching head in (b). The dark gray disc represents the sample position.

2.2.8 Polishing

After punching using the EDM, samples showed rough surfaces and where not suitable for fatigue testing as notches increase the stress locally. Thus samples were polished on the surfaces, as well as the edges.
Initially this was done using electro polishing in a mixture of 33% nitric acid and 67% methanol as used for transmission electron microscopy [34], although the methanol concentration was later increased to 72.5%. The set-up can be seen in fig. 31 and an electro polished sample in fig. 32(a). Noticeably the sample geometry suffers from this, as edges are especially affected by electro-polishing. Overall this method although resulting in the smoothest surfaces, caused irregular and hard to control surface geometries including width, thickness and curvature.
Samples of type *IS* as the baseline, as well as one set of *HPT@285℃* samples were prepared using this method to be compared to mechanically ground *HPT@285℃* samples. All other samples were prepared by metallurgical grinding. Samples were punched at a thickness of 0.25mm. After punching the edges were smoothed using P4000 polishing paper glued to a metal stick that was turned in the holes, periodically checking the edges using a light microscope. The two faces of the sample disc were subsequently ground using a P2500 and P4000 grinding paper consecutively, regularly checking the thickness in a light microscope. Finally a polishing felt was used, where care was taken that water was used sparsely to avoid oxidation. No polishing paste was used to prevent any reaction of the sample with it. Fig. 32(b) shows both an electro polished and mechanically polished sample.

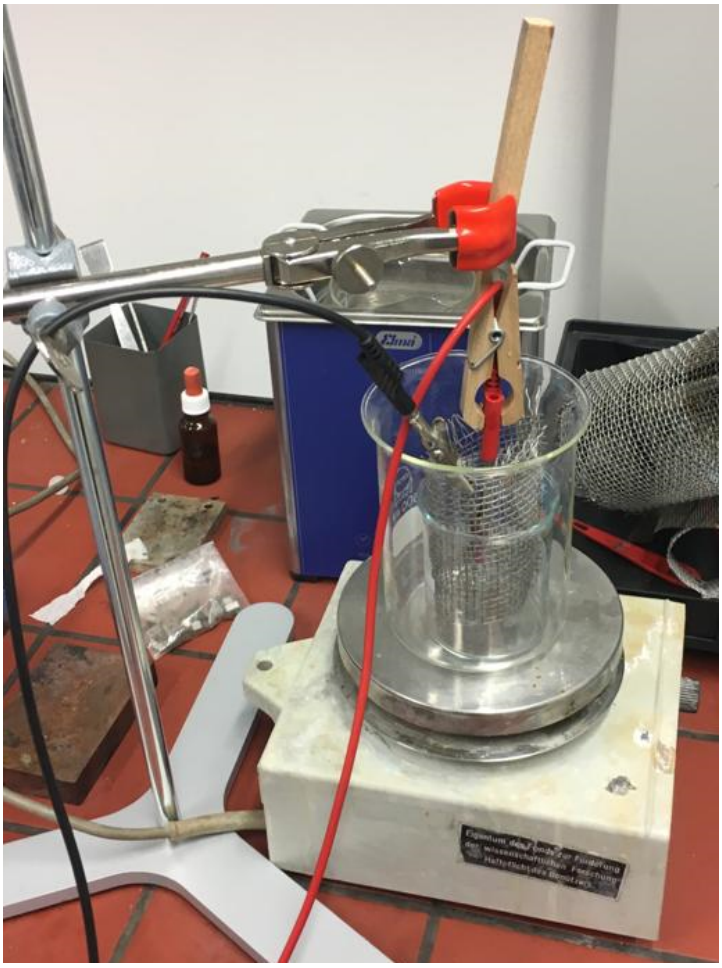

Figure 31: Set-up used for electro polishing.

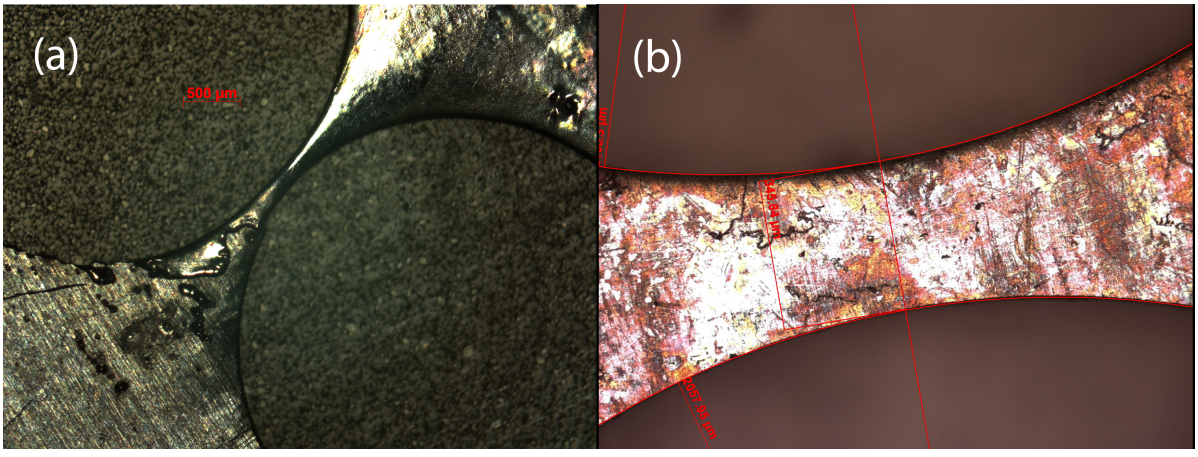

Figure 32: (a) electropolished *IS* sample resulting in deviating geometry, (b) mechanically polished *HPT@RT* sample.

2.3 Ultrasonic fatigue testing

As high cycles are needed to simulate the loading of skeletal implants an ultrasonic resonance fatigue testing system was used to reach loading cycles of 10^9 cycles in approximately 14 hours. The set-up consists of an ultrasonic generator, a piezoelectric converter, an acoustic horn and the sample holder. The piezoelectric converter converts the electric field created by the ultrasonic generator into a mechanical vibration with a frequency of 20kHz. This set-up can therefore be considered displacement controlled which results in a nearly constant strain amplitude. Software can be used to adjust the amplitude in a range from $30 - 90\%$ of the maximum output amplitude. Fig. 33 shows the different parts of the ultrasonic set-up. The length of the parts is chosen to be exactly half a wavelength of the excited wave. This achieves that the reflected wave has a phase shift of 180° and equal amplitude, thus creating a standing wave causing resonance in the specimen. The acoustic horn is important for achieving the desired amplitude as it sets the factor between the piezoelectric element and the sample holder depending on the different crosssections on both ends. For this an acoustic horn with ratio 1.23 : 1 was used for the *IS* samples and ratio 2 : 1 for all other samples. The extension horn is optional and was omitted. The whole set-up can be seen in fig. 34 and is constantly cooled with compressed air as the vibration causes the set-up to heat up. When the temperature increases the connection to the transducer worsens and the system tends to shut down. In addition heating of the samples can introduce systematic errors. Heating is caused by the dampening of the material used as the sample holder. The separate parts of the fatigue testing machine are screwed into each other and care needs to be taken to screw them on tightly, as they will otherwise vibrate uncontrollably, causing damage to the parts.

The sample holder can be seen in fig. 35. It is a bar shaped Ti-alloy ($Ti-6Al-4V$: $E = 113.8$GPa, $\nu = 0.342$, $\rho = 4.43\text{g/cm}^3$) with a $20mm \times 8mm$ crosssection and a length of 128mm. A hole with a diameter of 2mm is located at its center causing a maximum in strain. The sample is glued over the hole as seen in fig. 35 with a cyanoacrylate *HBM Z70* strain gauge glue. To ensure that the glue is thoroughly hardened, the sample holder is put into a vice shortly after glueing the sample on for a minimum of 6 hours. Care has to be taken that the sample is not pressed into the hole, which would cause it to bend as this results in a bending motion of the sample during testing rather than an uniaxial elongation. To circumvent this, pieces of rubber were put between the vice and the sample. The strain was measured by *HBM 1-LY11-0.6/120* strain gauges. Due to the size of the samples the strain gauge could not be glued directly on the sample,

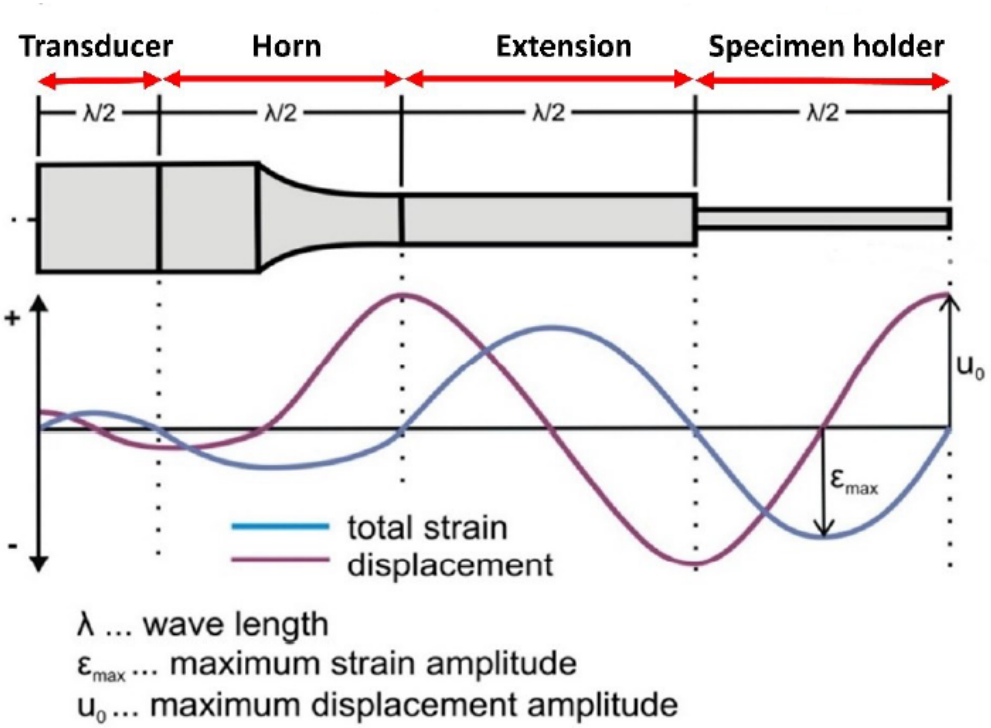

Figure 33: Schematic of the set-up used to test the fatigue behaviour of samples [33].

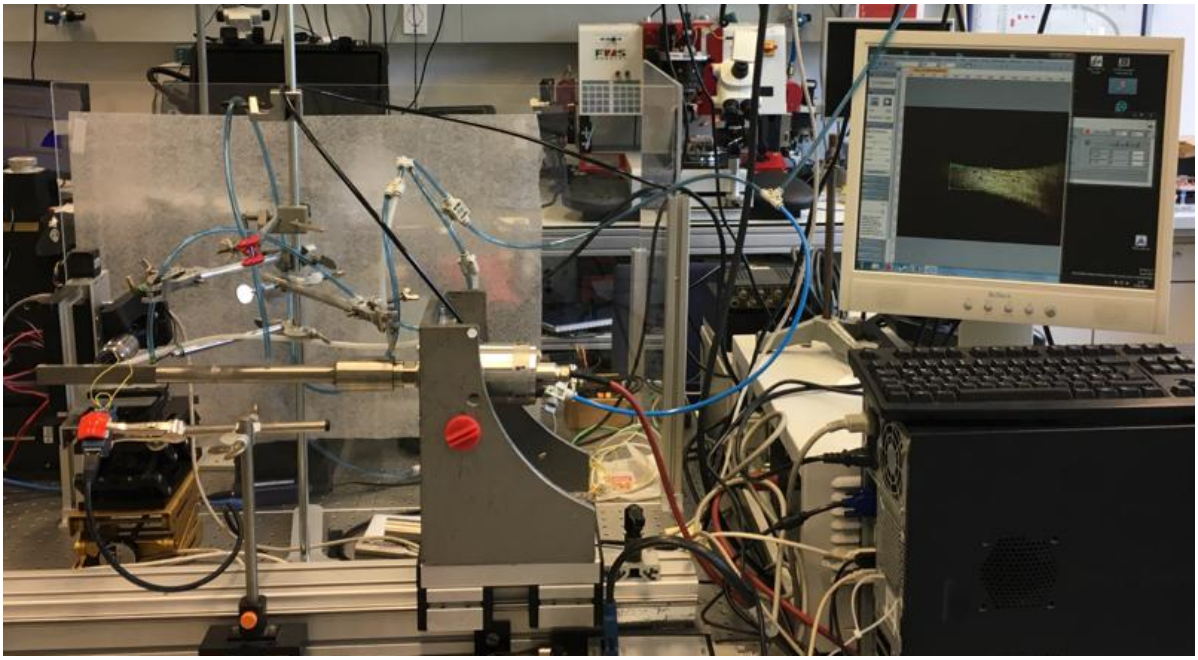

Figure 34: Set-up at TU Wien. The sample is connected to a strain gage and monitored by a microscope. Additionally it is constantly cooled by compressed air.

but was glued on the sample holder at the same hight as the hole at its side where the maximum stress occurred. Mounting the strain gauge this way however does not take the increase due to the sample geometry into account.

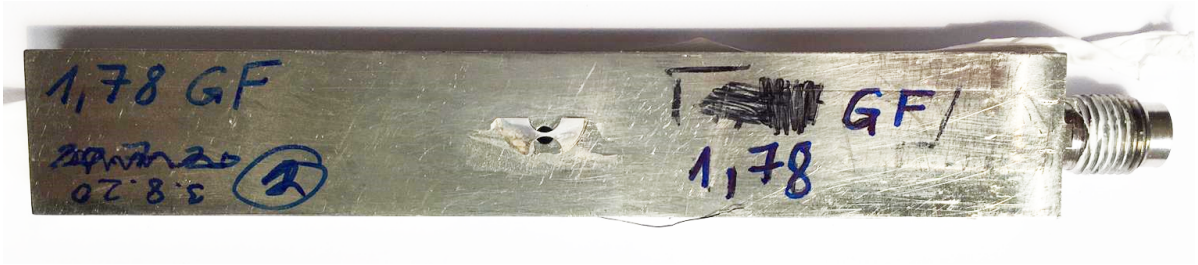

Figure 35: Sample glued onto sample holder prior to testing.

With this set-up it is not possible to monitor either hysteresis loops or hardening and softening of samples. Tests are performed at a load ratio of $R = -1$. Strain rates are in the μstrain range and are dominantly elastic, yet as discussed in chapter 1.4.3 irreversible effects lead to failure. The fatigue testing machine output the data that was measured in strain by the affixed strain gauges and had thus be converted into stress to plot as S-N plots. For this purpose, eq. 15 was used where $\frac{\Delta\sigma}{2}$ is the stress maximum and $\frac{\Delta\varepsilon}{2}$ is the strain maximum.

$$\frac{\Delta\sigma}{2} = \frac{\Delta\varepsilon}{2} \cdot E \cdot K_t \tag{15}$$

To analyse fracture surfaces the test has to be stopped quickly after failure as the two fracture surfaces of the sample collide with each cycle, thus destroying the initial fracture surface.

2.3.1 Effect of sample geometry

The final sample geometry is chosen for a multitude of reasons. As sample failure is measured by optical microscopy it is important that the sample breaks at the same point reliably. This is achieved by the hourglass shape where the middle is the area of maximal stress. Page 86 of [26] shows the influence of the notch in the present case. We have maximum width of the sample $H = 0.8$mm, notch radii $r = 2$mm, thickness in the middle $d = 0.35$mm and thickness $h = 0.2$mm. Thus In the case of ideal samples as seen in fig. 36 the stress concentration factor is $K_t = 1.055$. Page 307 of [26] shows a chart which can be used to calculate the stress increase due to the hole in the sample holder when using the values given in chapter 2.3. This results in a $K_t = 2.73$. Those two values have to be

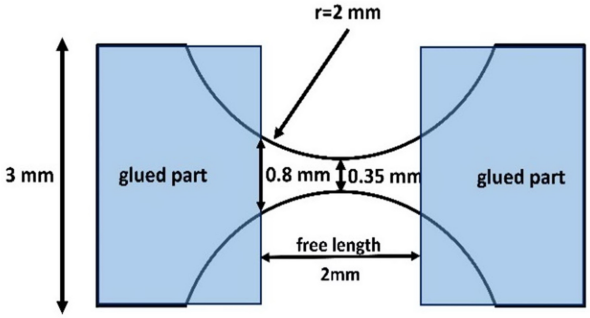

Figure 36: Schematic of the final sample dimensions [33].

multiplied to give the resulting stress increase that the sample experiences. Furthermore it is easy to spot samples with surface defects, when crack initiation occurs at a different place than near the smallest part of the sample. Such samples were discarded and not further analysed. Another important part to be considered when using micro samples for fatigue is the size effect, as nominal strength of a structure changes when scaling it. Dai et al. showed in [35] that the ratio $t/d = thickness/grainsize$ significantly influences the fatigue strength in HCF, where samples with higher t/d perform better under the same conditions than their counterparts with a lower t/d ratio. As grain size differs greatly between HPT at room temperature and at eleveated temperature, there is a factor 100 between the two ratios, $(t/d)_{R_T} = 875$ and $(t/d)_{285} = 8.75$. *HPT@RT* and *HPT@RT+HT* miniaturized samples can thus be considered to behave as bulk samples, whereas *HPT@285℃* and *HPT@285℃+HT* samples behave like very coarse grained samples.

2.3.2 Finite Element analysis

As described in chapter 2.3 the strain measurement was performed by a strain gauge not on the sample itself but on the sample holder.
One way to measure the increase in the stress due to the geometry and hole in the sample holder is to place a strain gage on the strained part of the sample and compare the two results. Simulations and [26] shows that the highest stress concentration occurs on the side of the sample and not its face, which would lead to additional errors.
Thus the increase in stress due to the sample geometry was considered by performing a finite element (FEM) analysis for samples of different crosssections to quantify the effect of sample geometry as well as of the hole, over which they were glued. For this ANSYS software was used defining a mesh of tetrahedrons and hexahedrons with 40659 vertices

in total. Focus was put on the area near the hole and the sample itself by refining the mesh there as seen in fig. 37. An external force is then applied, causing a displacement field which can be solved for vertices and is interpolated for edges with a 2nd order polynomial. As inputs the materials were considered to be isotropic and values for Young's modulus, poisson ratio and density for the samples (see chapter 2.2.6) aswell as for the sample holder (see chapter 2.3) were used. Additionally the crossectional area of the samples was considered. As this was one of the most senisitive parts of the geometry during preparation 3 different crosssectionial areas A were analysed using FEM and then plotted. If there is only a small deviation in the sample size a linear regression allows to choose individual values for K_t for each individual sample. As the Young's modulus for sample type *HPT@285℃* and *HPT@285℃+HT* is the same one simulation can be used for both types.

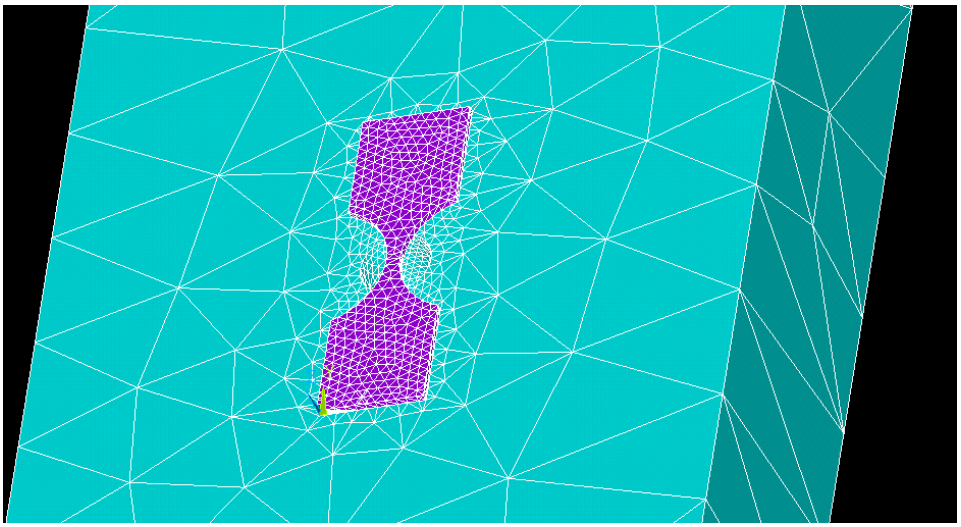

Figure 37: Mesh used to analyse the stress increase of the sample.

2.3.3 Vibrometer measurements

Thin samples subjected to cyclic testing experience buckling which describes the out of axis movement of the sample. To measure the magnitude of this effect a Scanning Laser Doppler Vibrometer (LDV) was placed perpendicular to the sample plane, in the front and back. LDVs measure the frequency shift of a laser beam reflected on the sample surface to that of the incident laser which gives information on the out of plane velocity and frequency. These values can be used to calculate the displacement of the sample and the sample holder. Furthermore having two lasers allowed to measure the

phase difference giving information on the change of the crosssectional area during cyclic testing.

2.3.4 Acoustic emission measurements

Although the end of the fatigue life of samples can easily be observed by means of optical microscopy during testing, it is impossible to determine internal changes shortly before and during cracking [36]. Acoustic Emission (AE) measurements are a good method to resolve internal changes with a high temporal resolution up to a few microseconds and can monitor the characteristic behaviour of different types of deformation types including twinning and collective dislocation movement. This is done with an ETA100 Ultra optical microphone by detecting the distinct energy release from the different forms of deformation [37]. Therefore a laser beam is emitted into a cavity bounded by two semi-transparent mirrors. Incoming sound changes the refractive index of the mirrors thus changing the intensity of the laser light, which in turn is compared to the initial intensity [36]. The incoming signal is split into discreet frequency bands via a Fourier transform. Using this technique, the evolution of resonance frequencies can be observed, giving good indication of the crack initiation before it becomes visible in the microscope.

2.4 Fracture surface analysis by electron microscopy

Fracture surfaces as well as the crack path can be observed and characterised using scanning electron microscopy (SEM).
For imaging a FEI ESEM Quanta 200 located at TU Wien was used. In addition interesting areas of sample surfaces were analysed by energy dispersive X-ray spectroscopy (EDX) to measure the elemental composition on the sample surface.

3 Results and Discussion

3.1 Stress and strain calibration

FEM simulations show the change in strain on samples, with a clear maximum at the narrowest part, as seen in fig. 38. Simulations were done by considering samples listed in table 3, which shows the values for K_t obtained for all sample conditions depending on their Young's modulus and their crosssectional area. These values were plotted and linearly fitted in fig. 39 and allow to factor the hourglass geometry of the samples as well as the hole in the sample holder over which they were glued into the S-N plots.
The change in K_t is measured as a function of the crosssectional area. In reality the change in thickness and width do not have the same influence on K_t. For exact analysis, which is beyond the scope of this work, K_t should be evaluated as a function of width and thickness independently. This can be seen when looking at sample *IS* #2, which has a crosssectional area of $width \cdot thickness = 408\mu\text{m} \cdot 181\mu\text{m} = 73848\mu\text{m}^2$. Although it has a crosssectional area close to the ideal $70000\mu\text{m}^2$ it deviates strongly from the linear relationship because width and thickness deviate strongly from the ideal parameters for the sample. This is an effect of [35] where more grains are in the crosssectional area of a wider sample for the crack to cross. Calculating K_t by using [26] severely underestimates the increase in stress caused by the set-up for all samples especially because the Young's moduli of the different conditions are not considered in this calculation.
Fig. 38 shows that the set-up results in a gradient of strain across the sample, with its maximum in the center of the sample at its lower surface (red color in in fig. 38).

Sample number	K_t **by FEM simulations**	K_t **by using [26]**	**Crosssectional area** A **[**μ**m²]**
HPT@285℃ #1	3.88	2.87	79881
HPT@285℃ #2	3.96	2.87	71110
HPT@285℃ #3	3.89	2.87	78601
$HPT@RT$ #1	3.77	2.85	84864
$HPT@RT$ #2	3.92	2.87	69426
$HPT@RT$ #3	4.02	2.87	58865
$HPT@RT + HT$ #1	3.71	2.88	85554
$HPT@RT + HT$ #2	3.97	2.87	63237
$HPT@RT + HT$ #3	3.94	2.87	68060
IS #1	3.73	2.88	88944
IS #2	3.8	2.87	73848
IS #3	4.2	2.84	42588

Table 3: Values for K_t and the crosssectional area for three samples, used in the linear regression as seen in fig. 39.

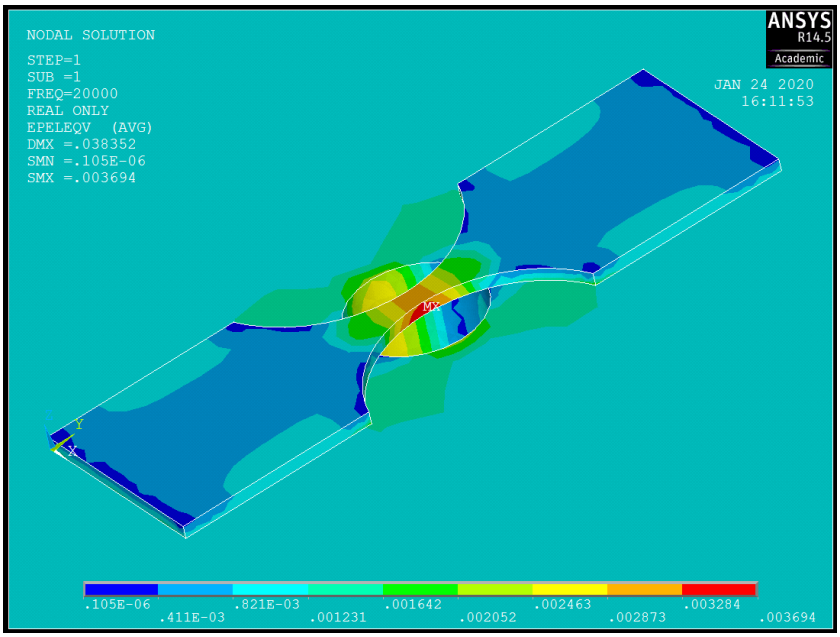

Figure 38: Strain distribution plot of *HPT@285˚C* #2 , showing the strain distribution as calculated by FEM.

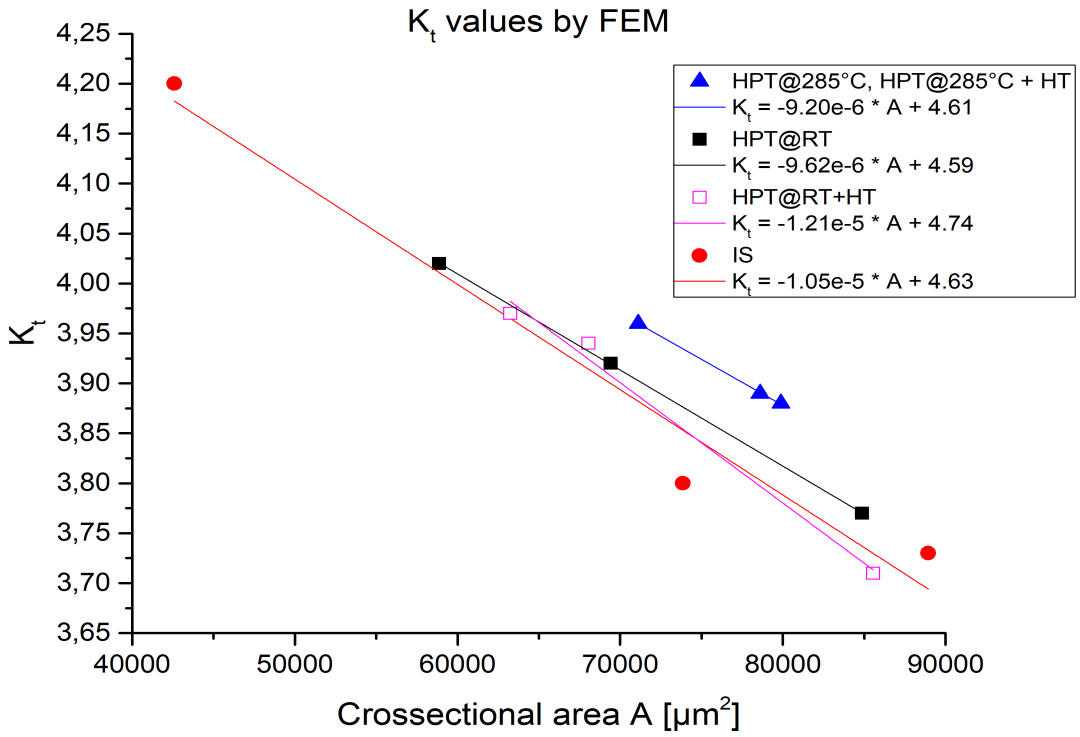

Figure 39: linear regression of K_t versus the crossectional area A measured by finite element analysis.

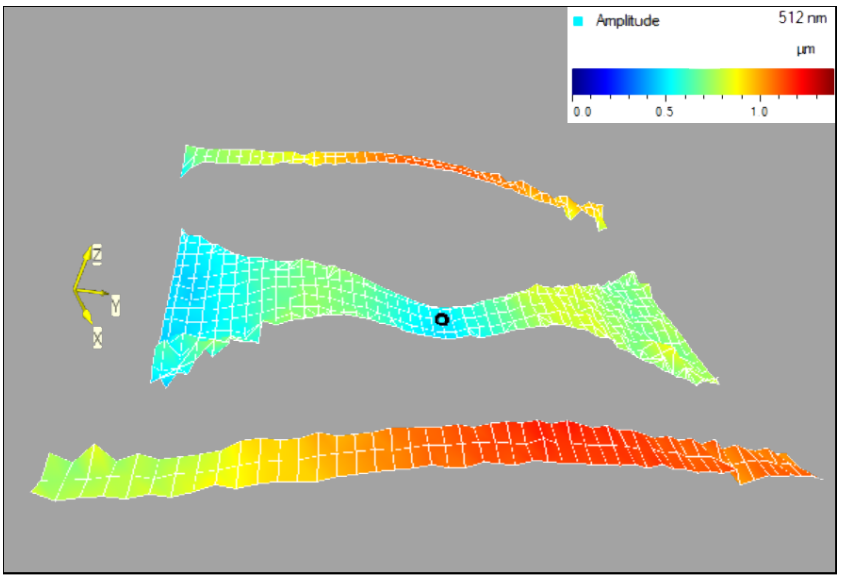

Figure 40: Exaggerated out of plane displacement of a sample during buckling. The stripes in the front and back show the behaviour of the sample holder. The maximum amplitude (512nm) is marked by the black circle.

3.2 Buckling and change in crosssection

LDV measurement was used to examine the out of plane movement and change in the crosssectional area during fatigue testing. Out of plane movement of samples impacts their fatigue behaviour and was thus analysed as shown in fig. 40. The maximum of buckling during the LDV measurement is 512nm relative to the unbuckled parts where the specimen is glued onto the sample holder and is marked by a black circle. An area to the sides of the sample on the sample holder was also analysed, which shows buckling of the sample holder too. Compared to the sample dimensions the influence of this out of plane movement is negligible and is not further considered in the analysis of the sample. To determine whether this movement was purely buckling or caused by a change in the crosssectional area, the phase shift between the two lasers used in the LDV set-up was measured as shown in fig. 41, and which is homogeneously at 111.7° at all points of the specimen and sample holder. For ideal buckling the phase shift would be at 180°, thus the specimens did experience a change in their crosssection, which increases the stress to failure of the samples. Considering the wavelength of the laser of $\lambda = 316$nm the change in width was calculated to be $\Delta d = 98$nm. As with the lateral movement, the change in thickness is small compared to the sample dimension and was thus not considered for further experimental results.

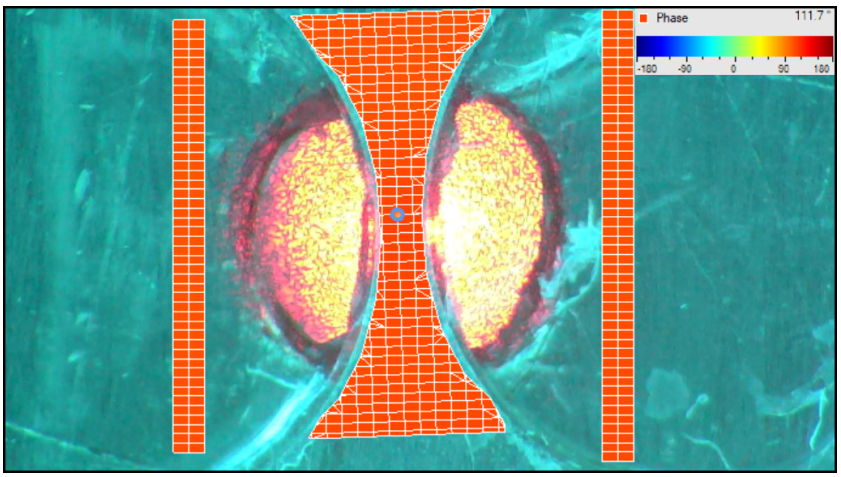

Figure 41: Phase distribution plot of the phase difference between the laser on the front and back of the sample and holder. The phase shown in the top right corresponds to the point marked by the blue circle.

3.3 Fatigue measurements

Results of fatigue tests can be seen in fig. 42 for all plots with a stress amplitude range from 0 to 250MPa and showing fatigue lifetime from $1e4$ to $1e9$. For easier visibility the more closely related sample conditions *HPT@RT* and *HPT@RT+HT* as well as *HPT@285℃* and *HPT@285℃+HT* are shown in fig. 43 and fig. 44 respectively. In fig. 44 the stress amplitude range that was plotted, was reduced to show a more detailed view of the plots. In all plots the fatigue behaviour of the *IS* sample is also given to show the relative increase in fatigue properties due to the different preparations methods. Data points marked by arrows indicate that the sample did not fail during testing. The vertical lines in fig. 42 are used to plot the ultimate tensile strength versus the fatigue resistance at $1e6$ and $1e9$ cycles for all different materials investigated. These results are shown in fig. 45 and fig. 46 respectively. In these plots, data from other sources is also included to allow for comparison to other magnesium alloys on the one hand, and other materials used as implants on the other hand.

To allow a comparison between the electro polished *IS* samples and the other samples it needs to be considered that when mechanically polishing samples, they experience a stress increase due to positive stress introduced on the surface. Furthermore there are changes in the geometry, especially the shape of the crosssection when electro polishing, that do not occur otherwise. To describe the effect caused by this, the 2 sets of *HPT@285℃* were plotted in fig. 47. The difference was measured by subtracting the trend line of the electro-polished sample from the mechanically polished sample. Fig.

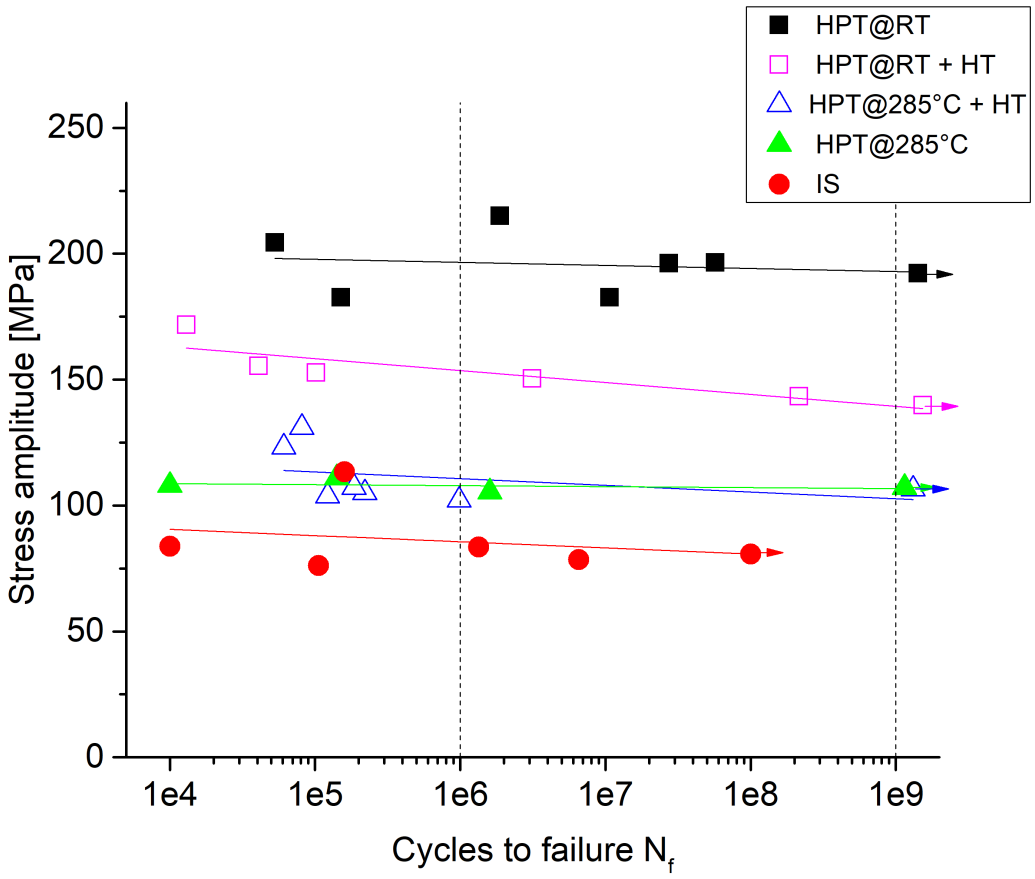

Figure 42: S-N plot of all investigated conditions. The colored lines indicate the trend lines for all samples. Dashed lines are points at which UTS versus fatigue strength was plotted.

48 shows this difference. This was then used to correct the plot of the *IS* samples, to allow it to be compared to the other conditions that were examined. The two different preparation methods do indeed show that electro polished samples have a lower fatigue resistance than their mechanically polished counterpart. There is also a difference in average crosssectional area of $A_{mechpol} - A_{elpol} = 16177.38\mu\text{m}^2$, although this effect should be corrected by including the K_t factor. Samples of type *HPT@285°C* showed consistent geometry regardless of the type of polishing, the samples of type *IS* however often suffered from a change in geometry, resulting in a deviation from the hourglass shape to a wire like shape. As the hourglass geometry with a higher K_t compared to thin wires, was assumed for all samples the more wire like samples likely show a higher fatigue strength. As the Mg5Zn alloy investigated in this work is intended to be used as implants, it is in constant contact with corrosive fluids and the fatigue properties are reduced drastically.

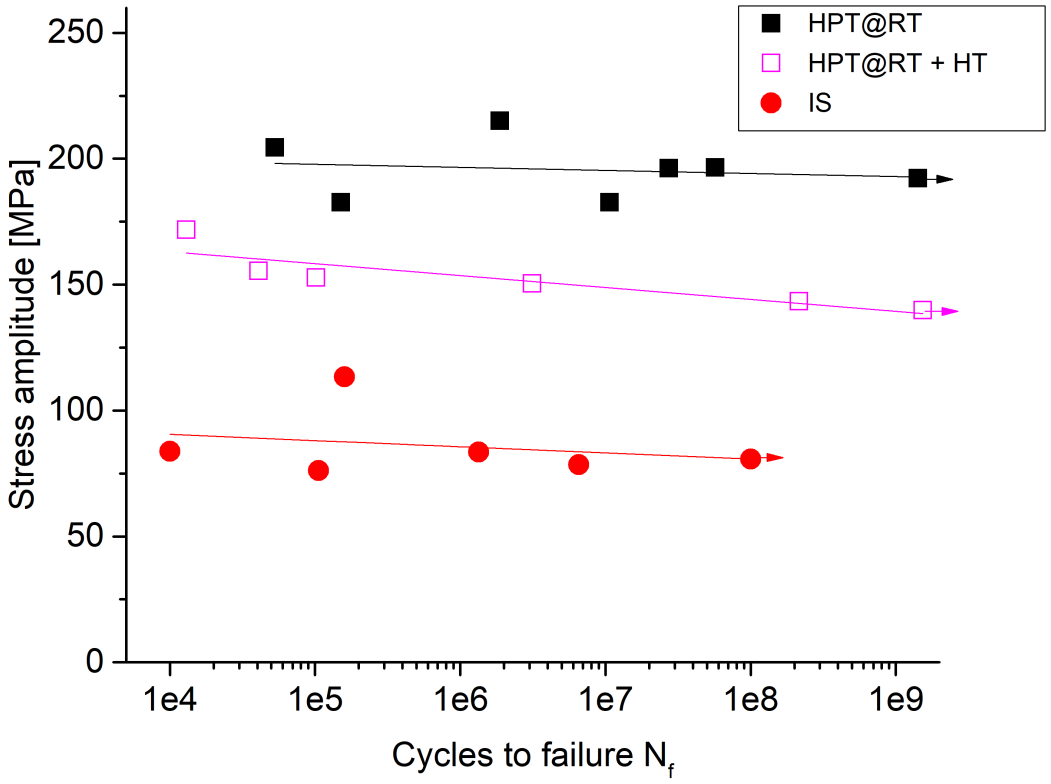

Figure 43: S-N plot of all investigated conditions which where HPT deformed at room temperature. *IS* condition is used to show the relative increase.

In [32] Ojdanic examined the corrosion properties of Mg5Zn, where the Zn causes an inhomogeneous corrosion where certain areas are missing after the tests and others are rather unaffected. Ojdanic further found that the different preparation methods did not significantly alter the materials corrosion properties. Therefore this influence can be omitted when comparing the fatigue resistance of the different conditions.
As implants from Mg5Zn studied here are intended for use as biodegradable implants after bone fracture, the region at around 1e6 cycles is of interest, as that for example corresponds to the average amount of load cycles an implant is exposed to during half a year of walking [41], where the average time for fractures to heal is up to 20 weeks [42]. In addition due to the degradation of MgZn in physiological contact, the implant is not likely to keep its structural integrity for longer than is necessary for the target area to heal [38]. The samples that were chosen as a comparison are shown in detail in table 4. For comparison MgZn-alloys were chosen as well as a TiNb alloy which was tested in a

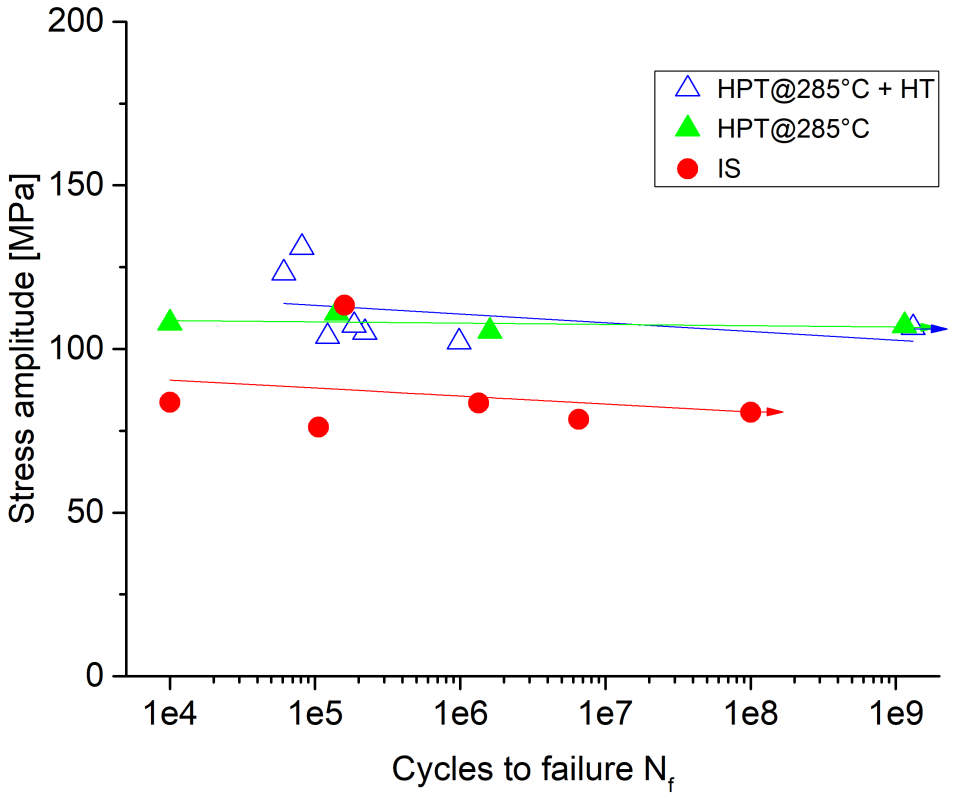

Figure 44: S-N plot of all investigated conditions which where HPT deformed at elevated temperatures. *IS* condition is used to show the relative increase.

coarse grained (CG) and an ultra fine grained condition (UFG), comparable to *IS* and *HPT@RT* respectively. Furthermore the TiNb sample had the same hourglass geometry as samples tested in this work. For useful comparison only samples with the same stress ratio of $R = -1$ can be considered.

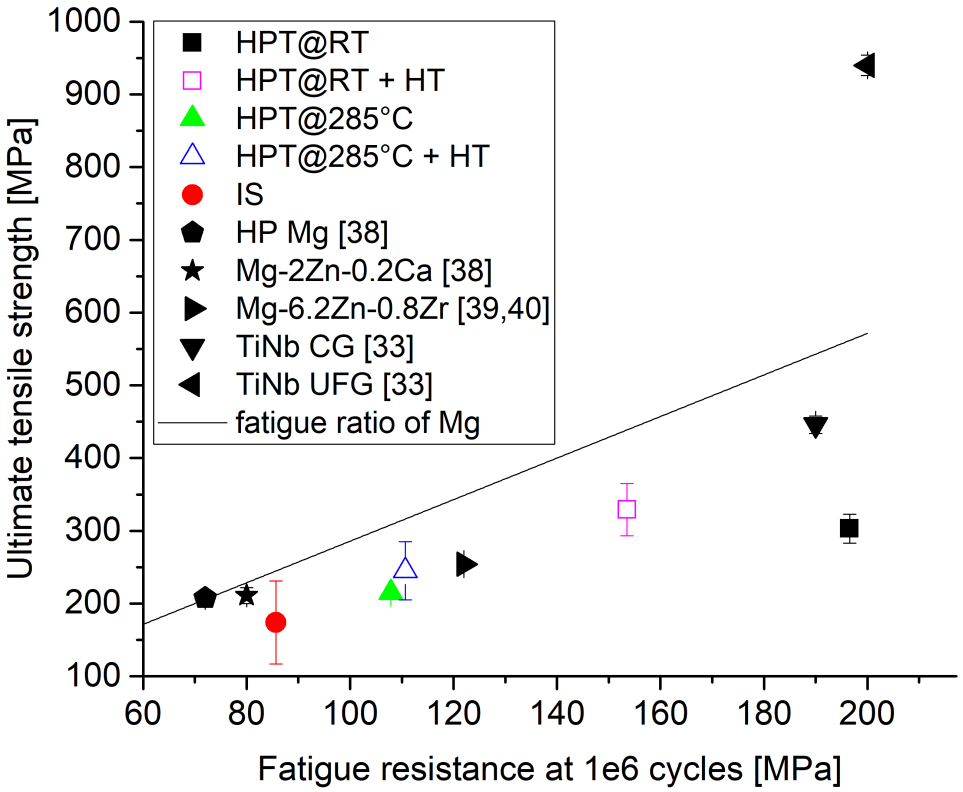

Figure 45: UTS versus fatigue resistance at 1e6 cycles to compare different conditions and materials. HP Mg and Mg-2Zn-0.2Ca data is taken from [38], Mg-6.2Zn-0.8Zr is taken from [39] and [40] and TiNb CG and UFG are taken from [33]. If no error bar is shown it is within symbol size.

composition	**Bulk sample**	**frequency** $[Hz]$	**grainsize** $[\mu m]$	**source**
99.99% Mg	yes	10	no data available	[38]
Mg2Zn0.6Ca	yes	10	no data available	[38]
Mg6.2Zn0.8Zr	yes	20000	$1-10$	[39] [40]
Ti-45Nb UFG	no	20000	< 0.1	[33]
Ti-45Nb CG	no	20000	20	[33]

Table 4: Details on the external data used for comparison with data obtained in this work, for all samples the stress ratio is $R = -1$ and all were mechanically polished.

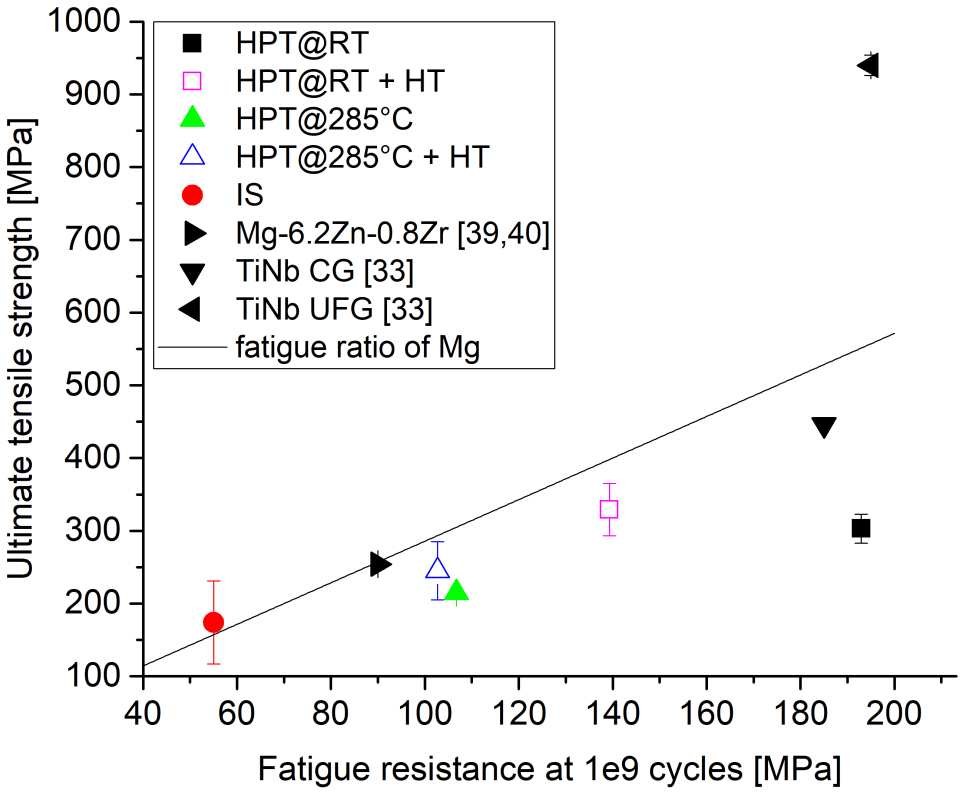

Figure 46: UTS versus fatigue resistance at 1e9 cycles to compare different conditions and materials. Mg-6.2Zn-0.8Zr is taken from [39] and [40] and TiNb CG and UFG are taken from [33]. The value for the *IS* state is taken by extrapolating the trendline. If no error bar is shown it is within symbol size.

For comparison of samples from studies done by [38] at 10Hz the frequency effect needs to be considered. This effect causes samples to exhibit a higher fatigue resistance at ultrasonic frequencies [43]. When comparing to samples from [38] it is important to consider the onset of the fatigue limit which appears at lower number of cycles for tests done at 20kHz than when using low cycle fatigue [44].

Another important aspect are the sample dimension and additional preparation methods. Bulk samples show a higher nominal fatigue strength than their miniaturized counterparts at same conditions (compare chapter 2.3.1). Especially when comparing the coarse grained miniaturized specimen (*HPT@285℃* and *HPT@285℃+HT*) to bulk samples they have a significantly different behaviour. Samples from [38] and [39] were mechanically polished bulk samples [45][40], thus increases in stress exist in all samples

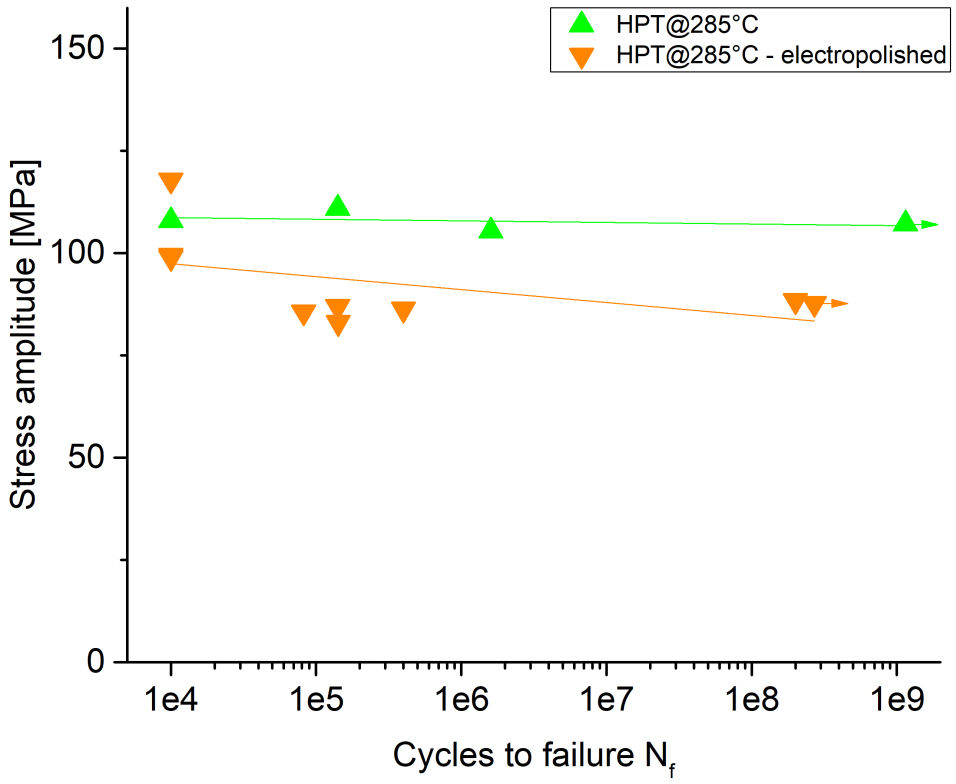

Figure 47: The change in stress amplitude of *HPT@285℃* samples which were previously electro polished or mechanically polished.

although this effect is smaller for bulk samples as they do not spend the majority of their lifetime in the crack initiation stage and their surface is a relatively smaller part of the sample volume than for miniaturized samples.

Fig. 42 shows the obtained S-N plots for all sample conditions that were tested. Samples deformed at room temperature show an increase in fatigue resistance by upwards of 100MPa compared to the *IS* material, while the fatigue resistance of samples deformed at elevated temperatures only show an increase of 20MPa. Evidently the reduced grain size and increase in hardness of the *HPT@RT* and *HPT@RT+HT* conditions are beneficial for the fatigue life of the magnesium samples.

IS miniaturized samples behave worse than HP Mg and MgZnCa (both extruded) bulk samples from [38] when considering the earlier onset of the fatigue limit due to the different frequencies used in the two works. *IS* was not expected to have good fatigue properties as this condition is in a supersaturated solid solution state and has large

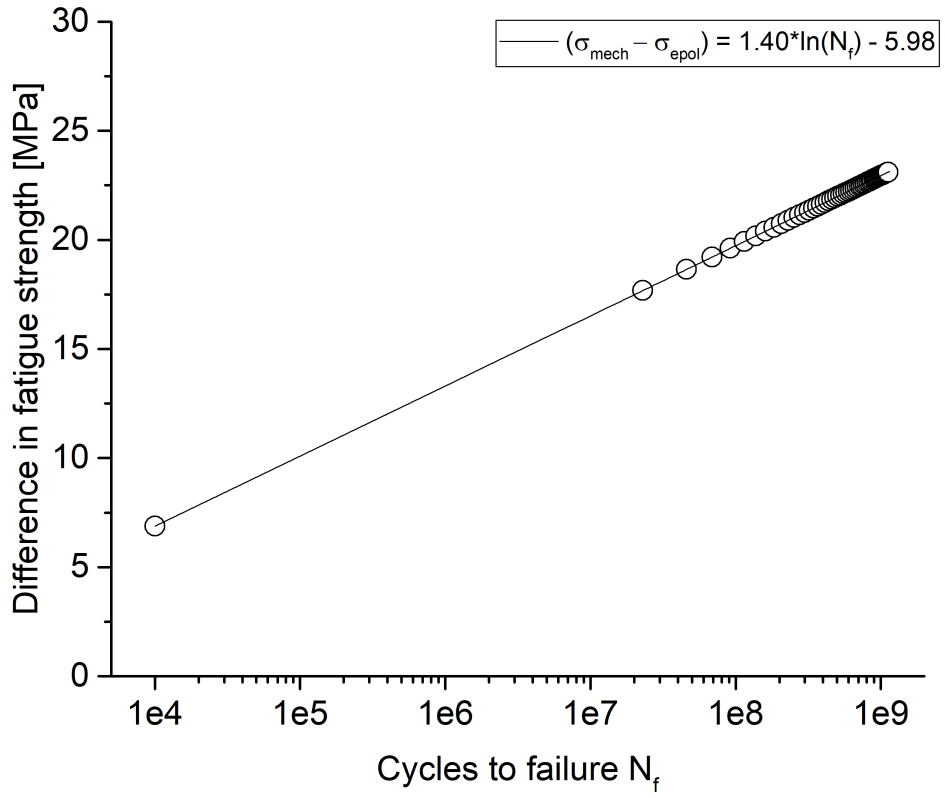

Figure 48: Approximation of the difference between electropolished and mechanically polisched samples.

grains therefore it neither experiences hardening due to precipitation hardening nor grain refinement. In [38] Bian et al. mention that extruded Mg behaves better than as-cast materials.

Samples deformed at high temperature only show a slight increase in fatigue properties compared to the *IS* samples, with no significant difference before and after heat treatment. There does not seem to be a significant increase to the fatigue resistance in either *HPT@285℃* or *HPT@285℃+HT* due to precipitates formed in this condition. The fatigue resistance at 1e6 cycles is increased by 40MPa relative to the bulk HP Mg sample from [38] not considering the size effect. The grainsize of the hot deformed samples is comparable to that of MgZnZr samples used in [39] and shows overall very similar fatigue behaviour at 1e6 and 1e9 cycles, indicating that the precipitates act very similarly to the precipitates present in the as extruded MgZnZr alloy. At 1e9 cycles, although not relevant for implant usage, the fatigue resistance of samples deformed at high tempera-

tures is very similar to that at 1e6 cycles in contrast to the MgZnZr sample which has a decrease of fatigue resistance of 30MPa. Crack propagation in the samples deformed at high temperatures is slower than that of the samples deformed at room temperature because of differences in the grain size.
HPT@RT and *HPT@RT+HT* samples show by far the most increase in fatigue resistance when compared to the initial material, where the samples that were heat treated have poorer fatigue properties. In UFG materials the crack propagation is very fast, thus the lifetime dependant property is the resistance to crack initiation at the surface. Apparently the vacancy agglomerates act as either stress concentrations thus allowing for a faster crack propagation and lowering the fatigue properties or cause softening of the material especially as both have a comparable Young's modulus, UTS, yieldstess and grain size. Especially at higher number of cycles the difference gets more significant as can be seen when comparing the fatigue resistance at 1e6 cycles shown in fig. 45 and the fatigue resistance at 1e9 cycles shown in fig. 46. Comparing these two conditions to the HP Mg and other Mg-alloys from [38] and [39] shows the significant positive impact of HPT deformation on the properties of the material compared to extruded materials. TiNb from [33] was chosen as it allows a comparison between a non HPT deformed sample and a HPT sample. In the case of Mg the increase of fatigue resistance is significantly higher than for the TiNb samples. Here the change in grainsize is far higher from *IS* to *HPT@RT* than it is from CG to the UFG condition but the change in fatigue resistance from 1e6 cycles to 1e9 cycles is less than in the Mg5Zn alloy. Both of the conditions deformed at room temperature surpass the Young's Modulus of bone by around 20GPa which can cause stress shielding. In this aspect the samples deformed at elevated temperatures are superior to those deformed at room temperature.
In surgical short-time devices for use in orthopaedics it is required that samples withstand a stress of $20 - 25$MPa when expecting a lifetime for about 5e5 cycles [41] [38]. All samples tested in this work fulfil this requirement.
The fatigue ratio, the ratio between fatigue strength at 1e8 cycles and the UTS for samples is given in table 5 and gives information on how the different preparation methods affected both non cyclic and cyclic mechanical properties. The literature value for the fatigue ratio for Mg is 0.35 [46] which is a good fit for the *IS* condition as well as both heat treated conditions at 1e9 cycles, which both have a very similar fatigue ratio. Interestingly at 1e9 cycles the samples that were deformed by HPT but not heat treated also show a very similar fatigue ratio which surpasses the expected value. At 1e6 cycles the fatigue ratios for all samples are approximately the same as at 1e6 cycles with the

only exception being the *IS* condition, which indicates that the extrapolation might not ideally fit.

condition	**fatigue ratio σ_f/UTS at 1e6 cycles**	**fatigue ratio σ_f/UTS at 1e9 cycles**
IS	0.49	0.32
HPT@RT	0.65	0.64
HPT@RT + HT	0.47	0.42
HPT@285℃	0.50	0.50
HPT@285℃ + HT	0.45	0.42

Table 5: Fatigue ratio for different condition.

3.4 Internal changes prior to failure

AE measurements were performed on multiple samples, although this was only used for a qualitative analysis during fracture and not done excessively enough to quantify the primary deformation mechanism as described in chapter 2.3.4. Fig. 49 shows the constant signal shortly before cracking in area (a), the burst signal typical for short events such as crack initiation in region x and the signal after cracking in region (b) with high time resolution. Fig. 50 shows the Fourier transform of the signal at the two stages (a) and (b). The signal at 20kHz is the external frequency imposed onto the sample from the ultrasonic fatigue testing machine. This allows a good temporal mapping of the events that occur in the sample.

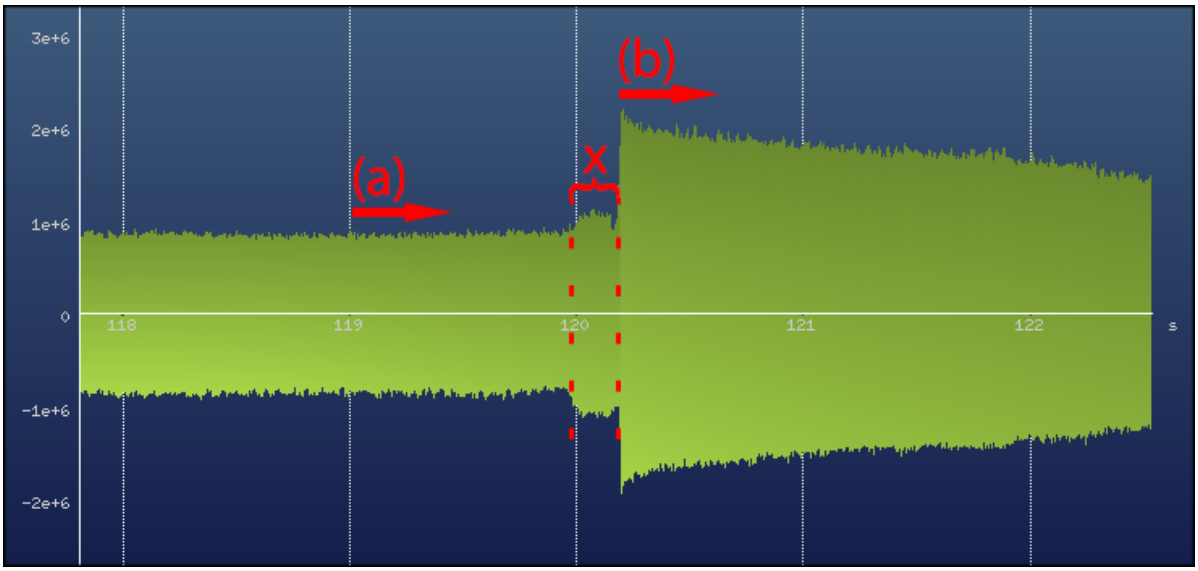

Figure 49: Signal as received from AE before, during and after cracking.

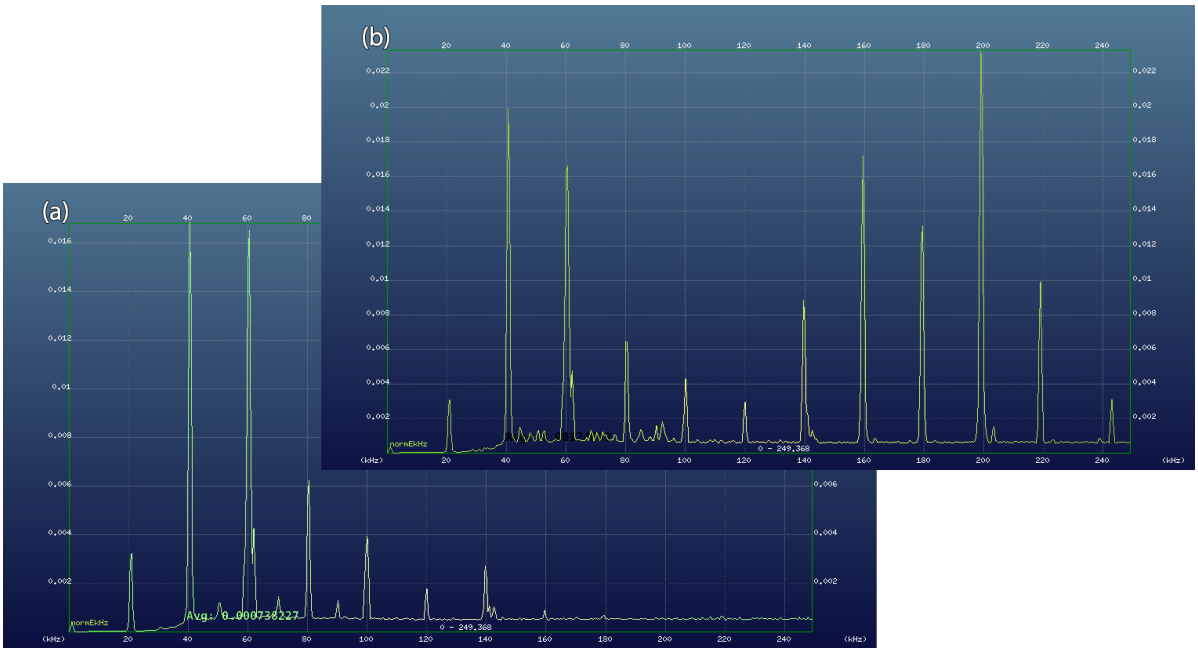

Figure 50: Fourier transform of the input signal before cracking (a) and after cracking (b).

3.5 Fracture surface analysis

Light microscopy was used to analyse the fracture path of the different conditions investigated in this work as shown in Figs. 51 - 55. All samples show oxidation due to the time between fatigue testing and crack path imaging, additionally fig. 51 shows the difference in the crosssection between front and back in fig. 51(a) and (b), which was a common issue when punching all holes simultaneously with EDM. Cracking occurs perpendicular to the strain direction, at the bottom of the sample, as seen in all light microscopy images, which is also suggested by the FEM results. In contrast to the other crack paths the sample in the *IS* condition shows a very similar crack path on both sides. Condition *HPT@285℃* shown in fig. 52 shows a very different behaviour on side (a) and (b), where the crack path is relatively straight in the first and very serrated in the latter. Considering this conditions grain size, the crack path in (b) seems to be more typical than the one in (a). Comparing to the SEM image of this sample in fig. 57 the crack initiated closer to the surface of the sample shown in fig. 52 (b), where it had a lower propagation rate and thus showed transgranular cracking. Closer to face (a) in fig. 52 the crack was faster and thus the crack was intergranular. Very similar behaviour can be seen in fig. 53, which had very similar behaviour concerning, grain size, fatigue properties and elongation to failure in tensile tests. Here too, the more serrated crack path in the face shown in fig. 53(b) is closer to the crack initiation site in the SEM image shown in fig. 58.

In fig. 54 the crack path for the *HPT@RT* sample is shown, which shows a much smoother crack path than conditions *IS* and samples deformed at elevated temperatures, even though the crack path is not as smooth as expected for an ultra fine grained material. Furthermore the crack path does not show significant differences on either face (a) nor (b) which is in good correlation to the SEM images shown in fig. 59 where the smooth surface hints to a fast crack propagation throughout the whole sample.

The crack path for the *HPT@RT+HT* sample shown in fig. 55 shows a very smooth crack path in (a) but a very serrated one in (b) probably due to brittle cracking behaviour of the sample.

To analyse the fracture surfaces of all conditions, SEM images were taken. Fracture surfaces show the typical 3 regions observed during fatigue crack propagation. Region 1 is the crack initiation region, region 2 the steady crack propagation region and finally region 3 the area where final rupture occurs. Typical for cracking at these number of cycles is the crack propagation from one point of the surface inward (indicated with arrows in Figs. 56 - 60, where in this case, cracks propagate mainly from the side faces

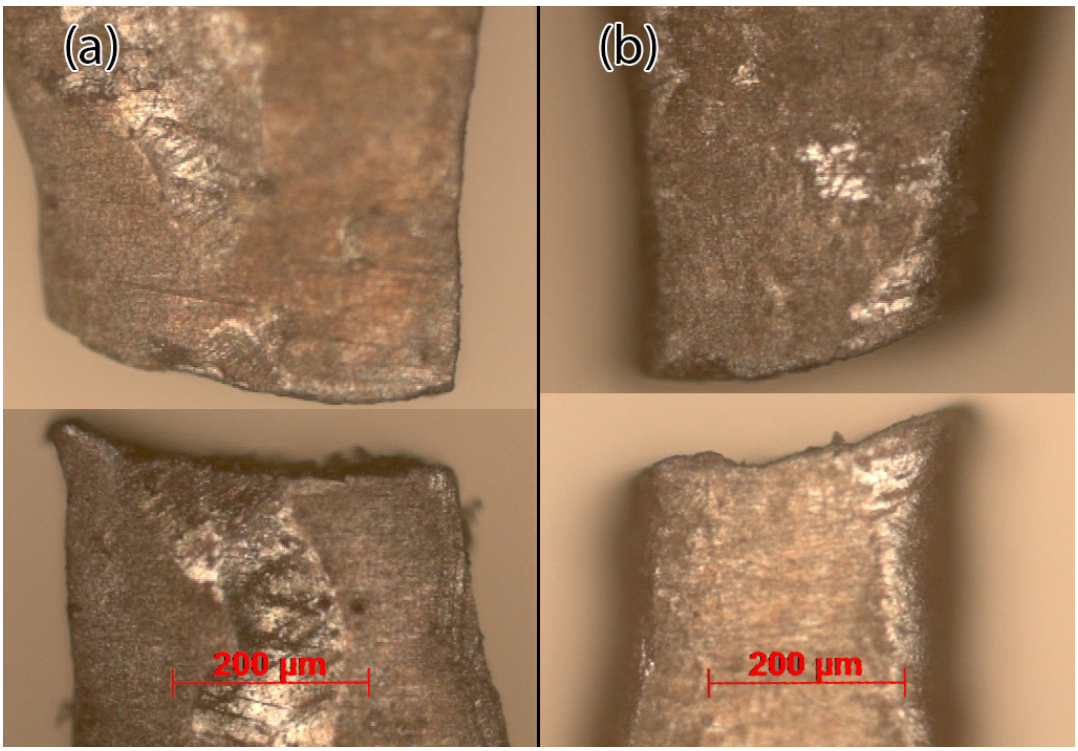

Figure 51: Light microscopy image of the fracture path of an *IS* sample on the front and back side.

not from the edges of the samples and show a smooth area, the only exception being the *HPT@285℃+HT* sample depicted in fig. 58 where the crack initiates at the corner. Fatigue striations are visible in all samples (fig. 57(b) and (d), fig. 58(b) and (d) and fig. 59 (b)). Spacing of fatigue striations is larger in samples deformed at high temperature than at low temperature which is an indication for faster crack growth in the conditions deformed at higher temperatures [47]. Only fig. 60 shows no fatigue striations but only secondary microcracks visible in region 1 and 2, which is typical for brittle fracture behaviour. Specimens deformed at room temperature are more brittle than the other conditions tested in this work, as seen in the work of Ojdanic [32] and hints towards the suppression of twinning. However sample *HPT@RT*, shown in fig. 59, does not show this microcracking behaviour, but instead fatigue striations. The sample depicted in fig. 57 shows an unusually large oxidized area (30wt% oxygen as measured by EDX) in region 2 with fatigue striations parallel to the crack propagation direction. Overall the appearance of fracture surfaces between specimens deformed at room temperature and those deformed at 285℃ differs significantly which can be attributed to the difference in grain size. Furthermore intermetallic MgZn particles are visible in all samples, while

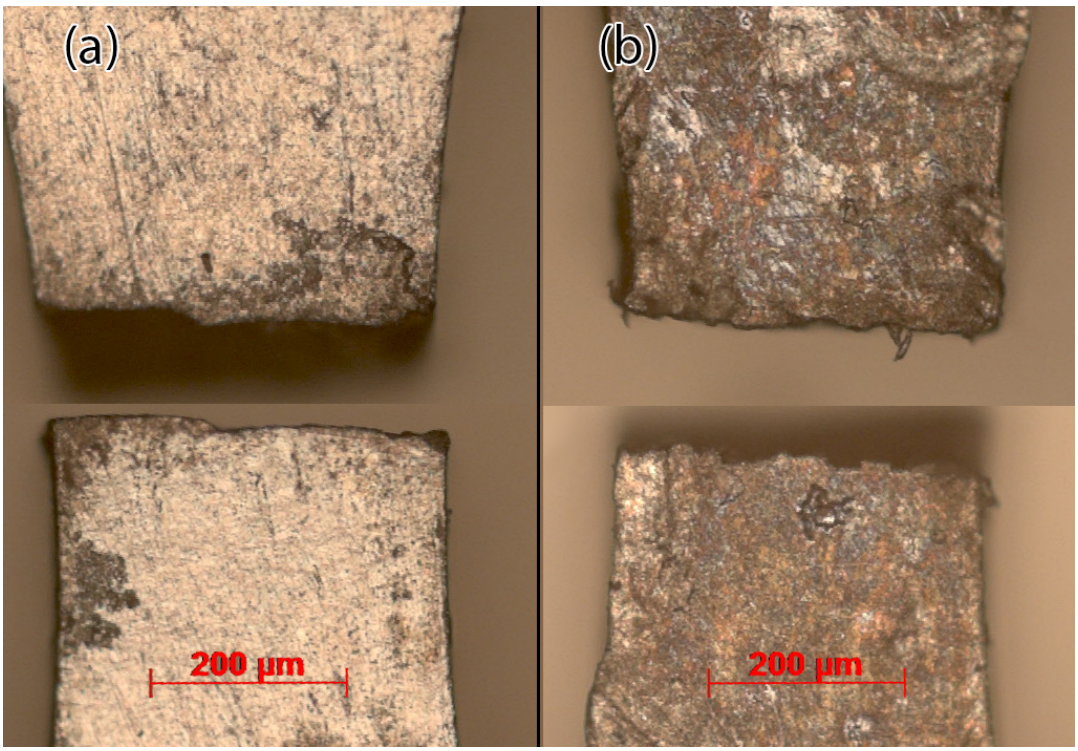

Figure 52: Light microscopy image of the fracture path of a *HPT@285℃* sample on the front and back side.

more pronounced in the samples deformed at room temperature. These are indicated by bright contrast compared to the rest of the surface. This is in good accordance to the work of Ojdanic in [32] describing a better supersaturated solid solution state by HPT deformation at elevated temperatures than by HPT deformation at room temperature. Although such precipitates can act as the initiation site for internal cracks at higher number of cycles in bulk materials, such as prosthetics, they are negligible in the usage of biodegradable implants, as in that case failure most often occurs due to corrosion pitting especially given the inhomogeneous corrosion behaviour of Mg5Zn. Fig. 59(c) shows granular structure with size in range of the grainsize of *HPT@RT* samples (compare table 2), which indicates intergranular cracking. The *IS* sample shown in fig. 56 also shows a brittle behaviour at the start of the crack in fig. 56(c) which is in a stark contrast to the ductile nature the material exhibited during tensile testing in [32]. Overall however, this sample exhibits a rougher surface morphology than the sample deformed at room temperature. However the sample surface does not show the typical surface seen for coarse grained materials as it is smeared because of external force exerted after failure, most likely because it was not removed from the ultrasonic fatigue set-up early enough.

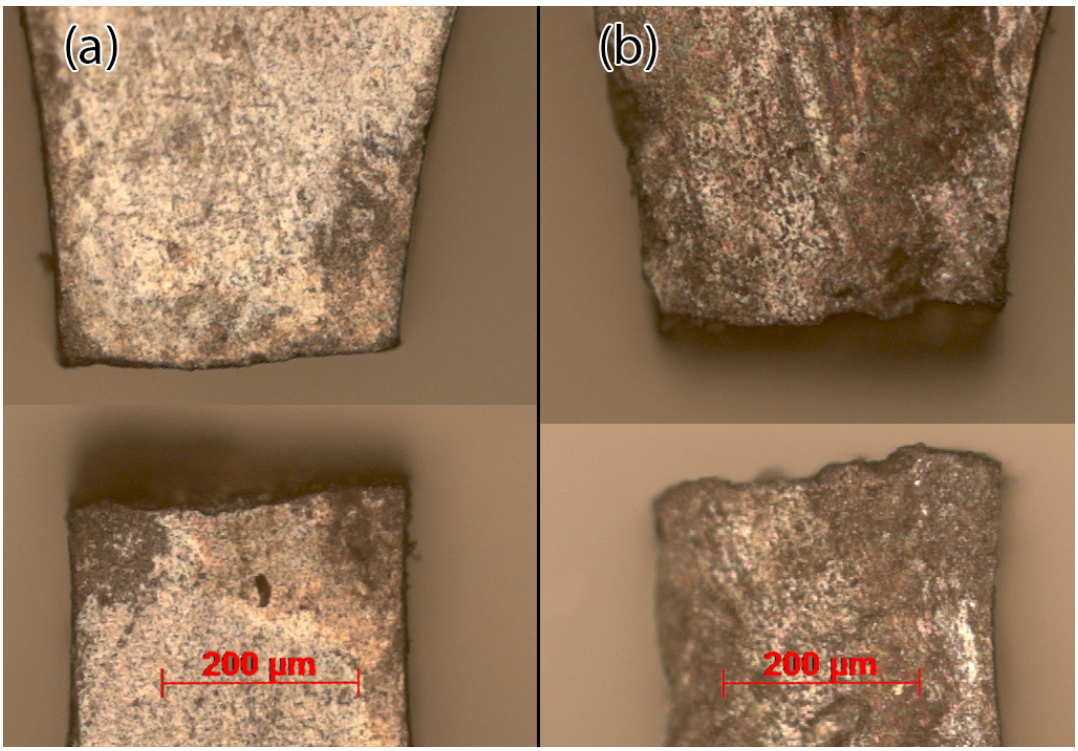

Figure 53: Light microscopy image of the fracture path of a *HPT@285℃+HT* sample on the front and back side.

EDX measurements revealed that the bright spots in fig. 56(b) and (c) are copper particles. These were most likely introduced during sample cutting with EDM.

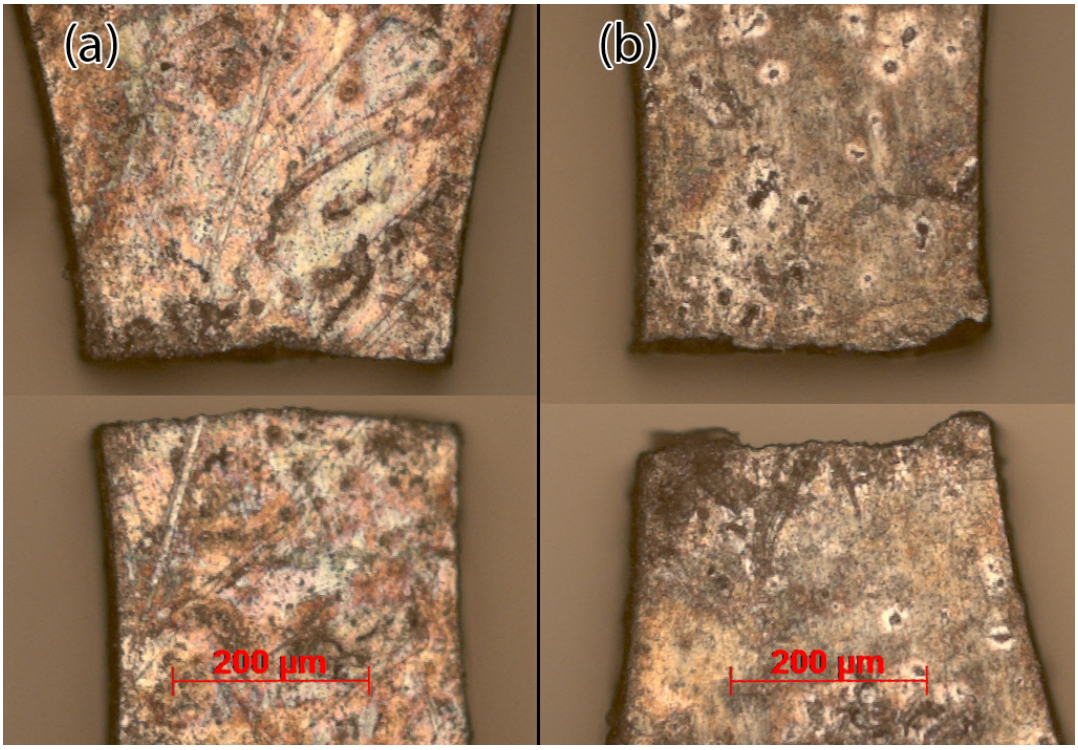

Figure 54: Light microscopy image of the fracture path of a *HPT@RT* sample on the front and back side.

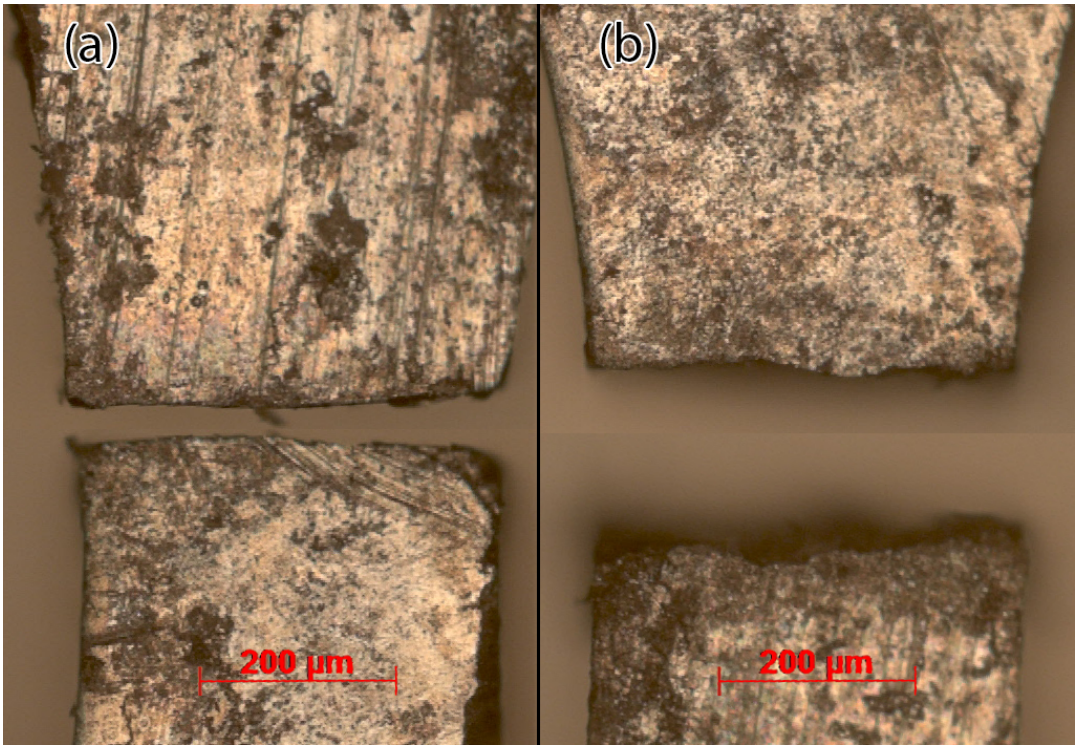

Figure 55: Light microscopy image of the fracture path of a *HPT@RT+HT* sample on the front and back side.

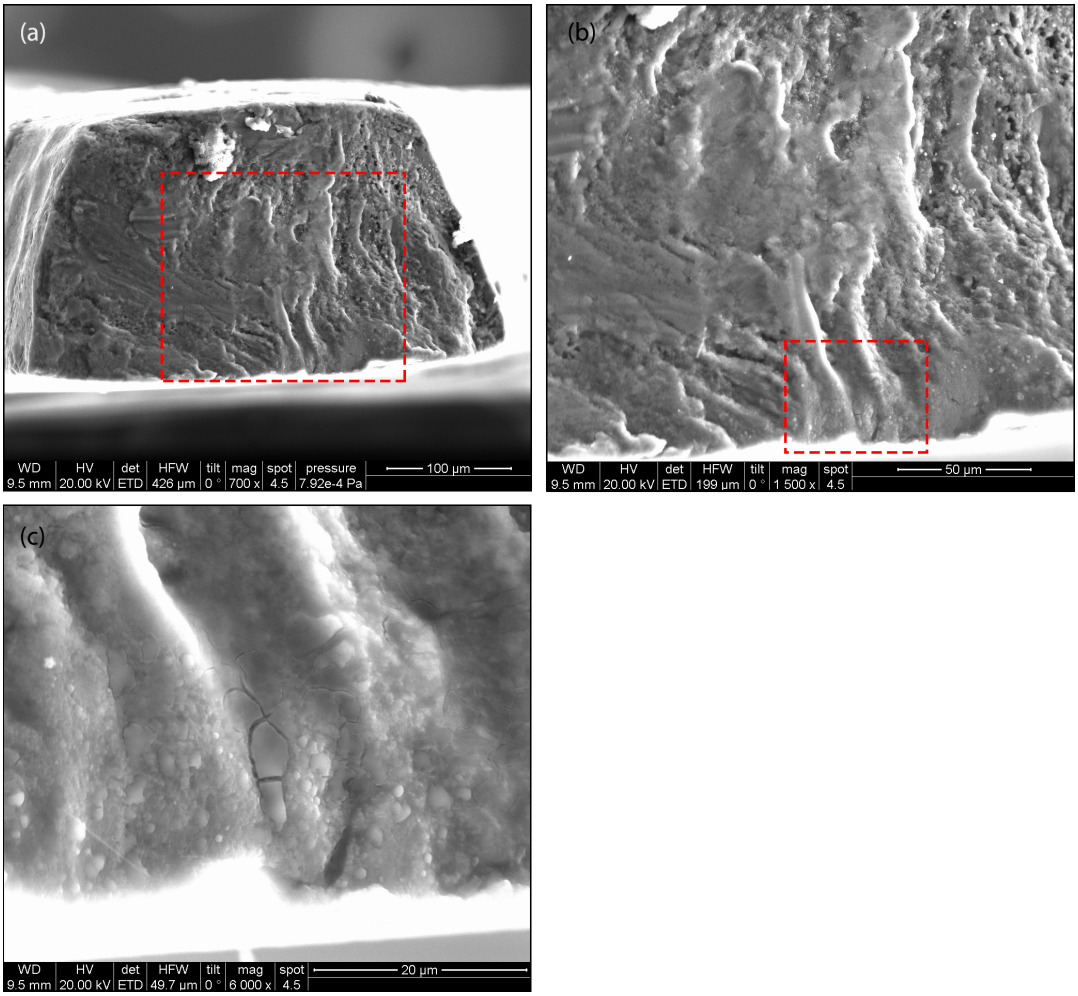

Figure 56: Fracture surface images of an *IS* sample. (a) shows the overview, with (b) and (c) taken at higher magnifications at the points indicated by the red rectangles. Bright white spots in all three images are external contaminations that persisted after cleaning in acetone.

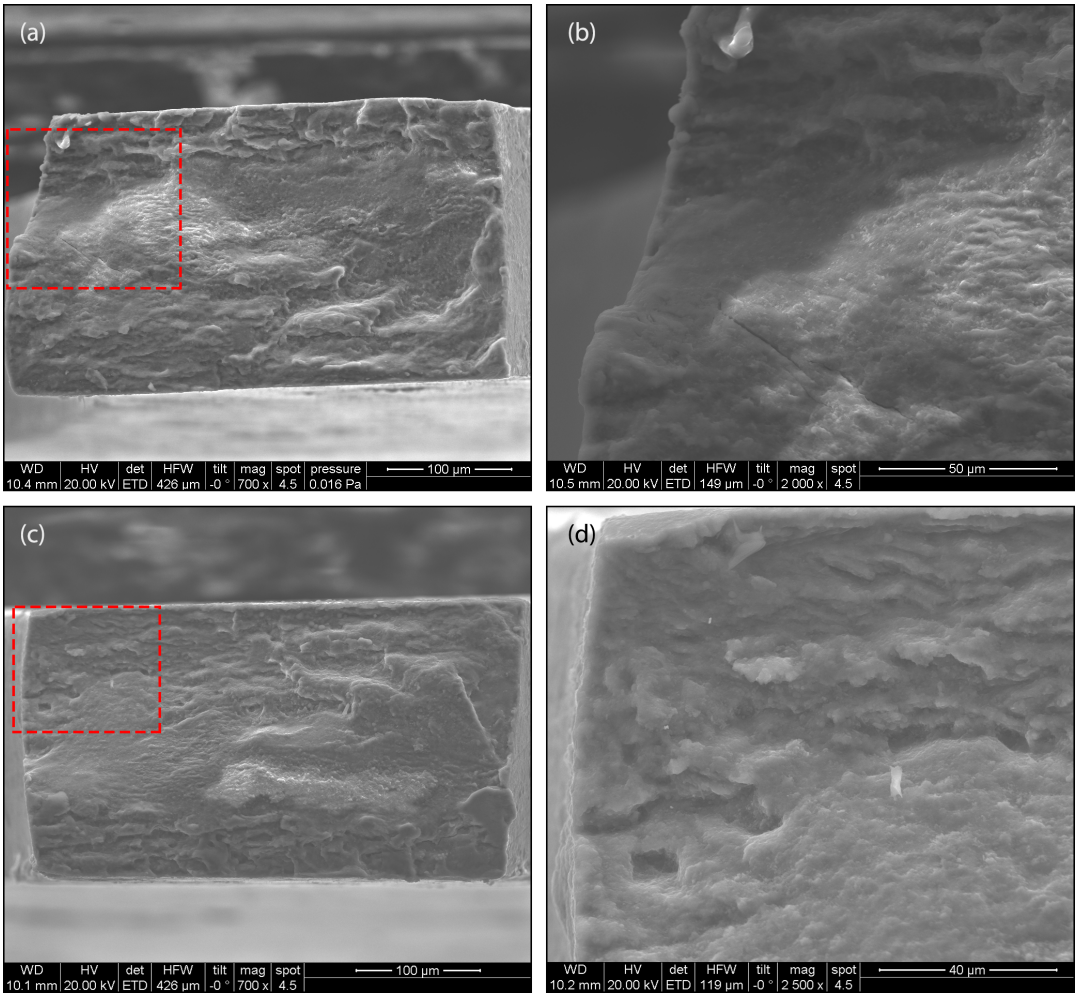

Figure 57: Fracture surface images of the two fracture surfaces of a *HPT@285℃* sample. (a) and (c) show the overview, with (b) and (d) at higher magnifications at the points indicated by the red rectangles. The bright white spot in the top left of the sample is an external contamination that persisted after cleaning in acetone.

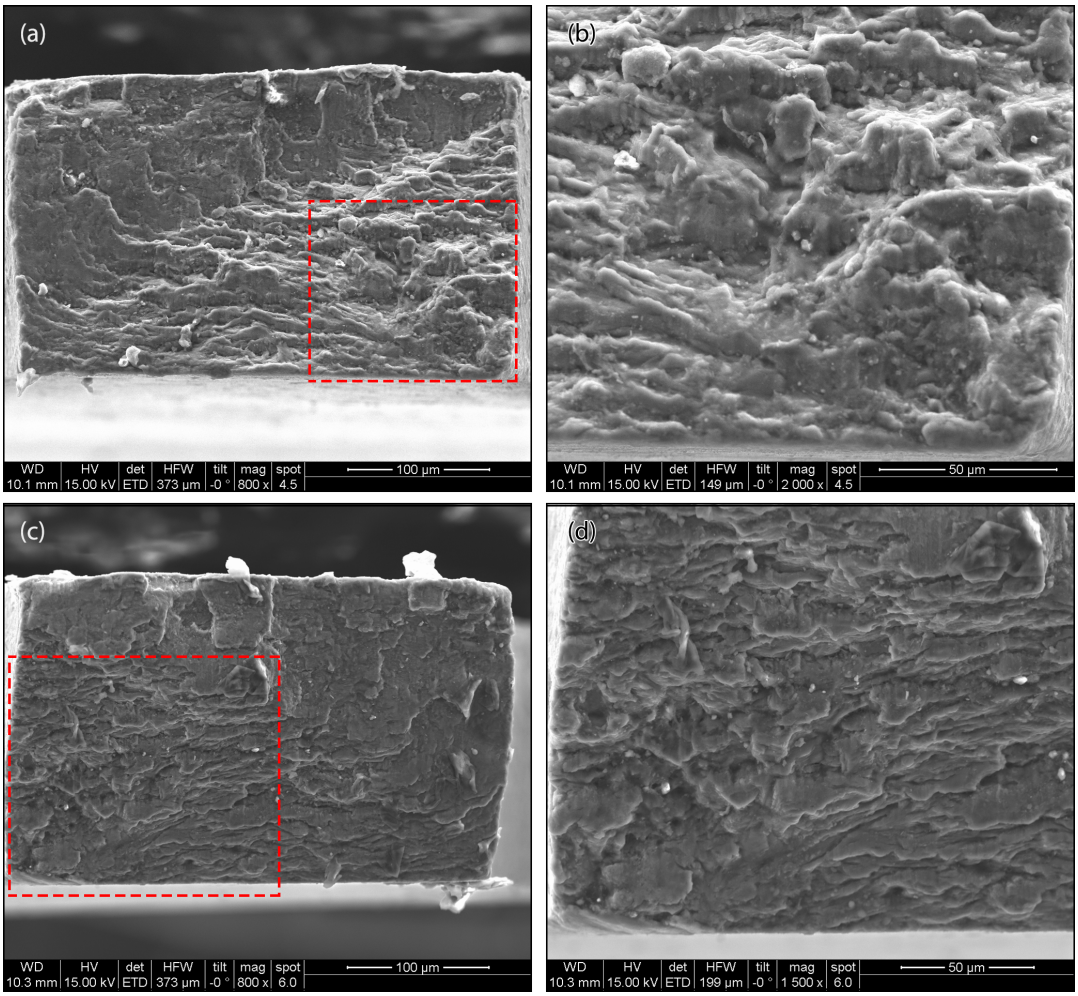

Figure 58: Fracture surface images of the two fracture surfaces of a *HPT@285℃+HT* sample. (a) and (c) show the overview, with (b) and (d) at higher magnifications at the points indicated by the red rectangles. Bright white spots in the bottom left corner of (a) and distributed over the sample surface in (c) are external contaminations that persisted after cleaning in acetone.

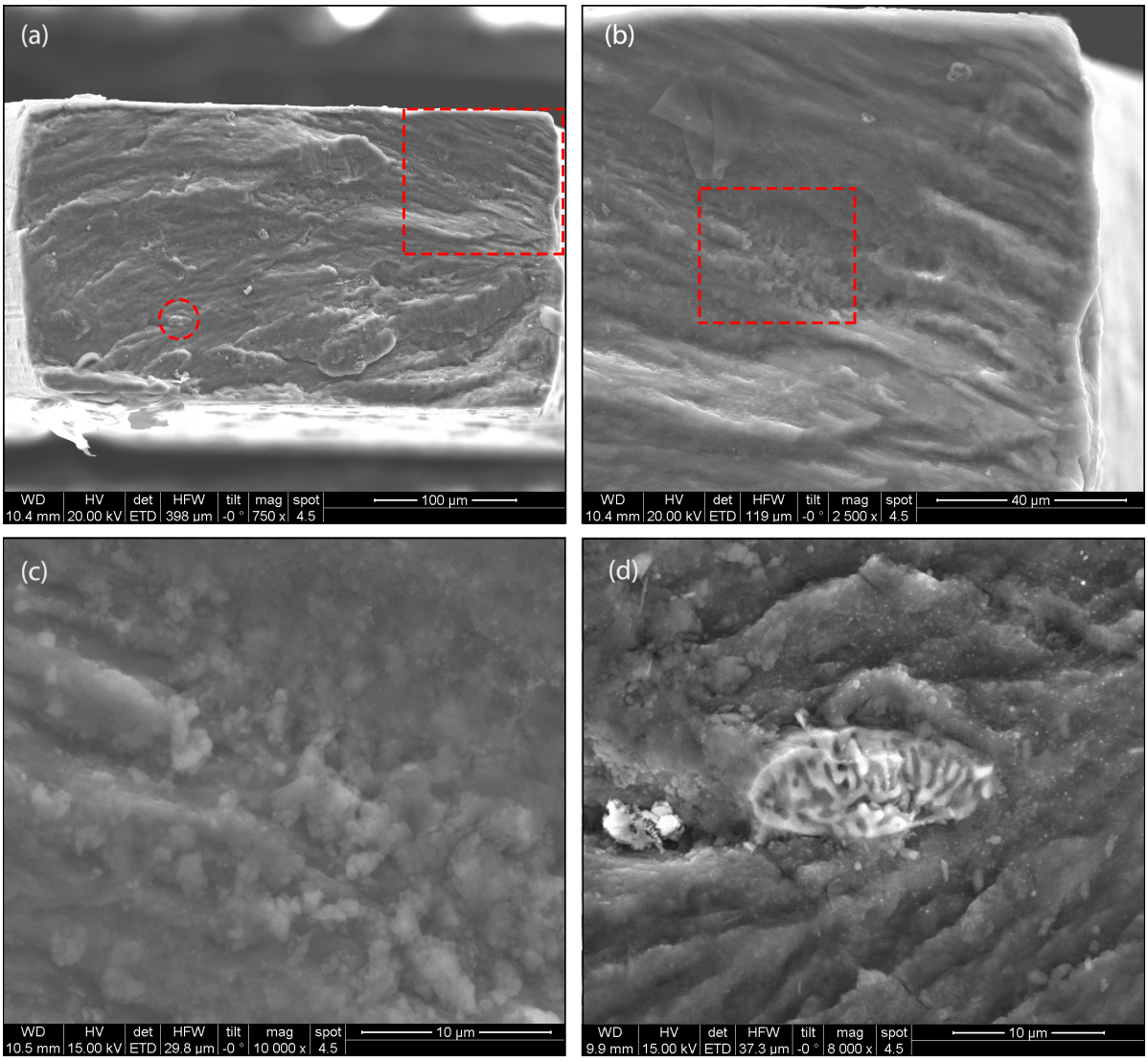

Figure 59: Fracture surface images of a *HPT@RT* sample. (a) shows the overview, with (b) and (c) taken at higher magnifications at the points indicated by the red rectangles. (d) shows a precipitate indicated by the circle in (a).

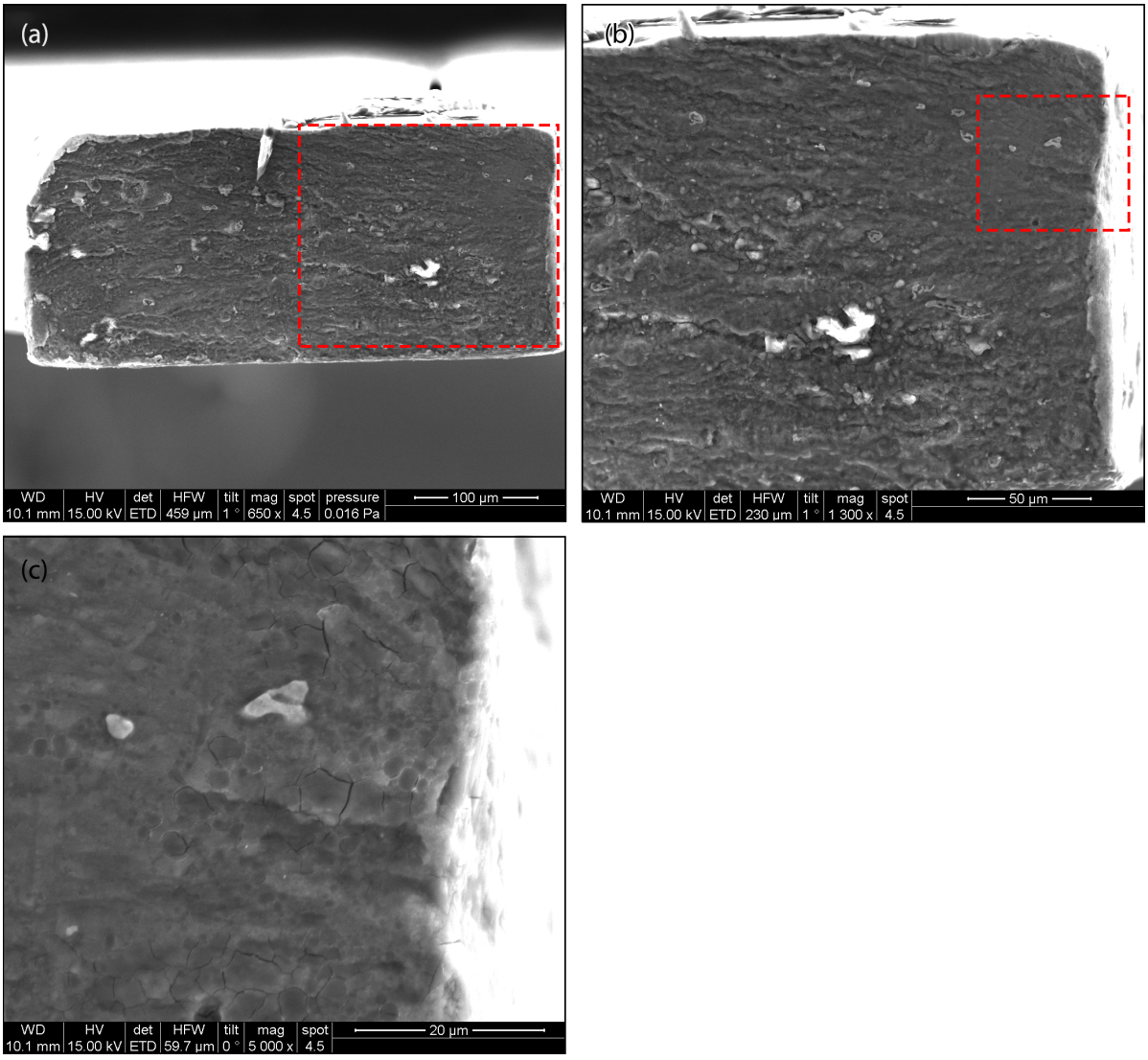

Figure 60: Fracture surface images of a *HPT@RT+HT* sample. (a) shows the overview, with (b) and (c) taken at higher magnifications at the points indicated by the red rectangles. Bright white spots in images (a) and (b) are external contaminations that persisted after cleaning in acetone.

3.6 Summary, conclusions and outlook

This work investigated the fatigue properties of a Mg5Zn alloy prepared in five different ways:

- homogenization at 350℃ of the sample for 24h abbreviated as *IS*
- homogenization at 350℃ of the sample for 24h and HPT deformation of 0.5 rotations abbreviated as *HPT@RT*
- homogenization at 350℃ of the sample for 24h, HPT deformation of 0.5 rotations and heat treatment in an oil bath at 100℃ for 24h abbreviated as *HPT@RT+HT*
- HPT deformation of 10 rotations at a temperature of 285℃ abbreviated as *HPT@285℃*
- HPT deformation of 10 rotations at a temperature of 285℃ and heat treatment in an oil bath at 100℃ for 24h abbreviated as *HPT@285℃+HT*

As samples were miniaturized due to the HPT deformation a special geometry had to be used for fatigue testing, which was realized by special tools also designed in the scope of this work. The special geometry was analysed with FEM and LDV methods for further detail and during fatigue testing AE measurements were performed. To prevent stress concentrations after sample preparation, samples were further prepared using either electro polishing or mechanical polishing. After failure the crack paths and the fracture surfaces were analysed for further detail on the behaviour of the different sample conditions.
The multiple tools that had to be designed and improved upon for sample preparation clearly shows the importance of this topic when considering ultrasonic fatigue measurements of miniaturized samples. It is not only important to achieve the desired thickness but also the proper square crosssection of the final sample. Optimally the sample preparation should be shifted away from EDM and be done by laser cutting which produces smooth surfaces without the need to polish the sides manually. If the samples are prepared by EDM machining the sample should be mechanically polished, on their faces and also their edges. This results in a better final sample shape when compared to electro polishing. Especially for Mg samples the rapid oxidation caused the sample quality to quickly deteriorate after electro polishing. For calculating the increases in the stress due to the special geometry FEM calculations allow a more precise calculation of the stress increase due to the sample geometry and set-up by including material constants

in contrast to measurements by numerical approximations where only the geometry is considered in the calculation. Lateral motion and change in crosssection during fatigue testing was investigated by LDV measurements, and no significant impact could be observed. Lateral motion of no more than 512nm and changes in thickness of only 98nm were measured.

Fatigue measurements showed that *HPT@RT* has the best fatigue properties of all sample conditions due to its nanocrystaline structure and high dislocation density. The creation of vacancy agglomerates within the material were not beneficial to the fatigue properties but most likely made crack propagation within the material easier causing a significant decrease in fatigue properties in the condition *HPT@RT+HT*. As the UTS and Young's modulus of both conditions deformed at room temperature are comparable this clearly favours the usage of the condition that was not heat treated for the use as biocompatible implants. The fatigue properties of samples deformed at elevated temperatures showed a significantly lower increase compared to the samples deformed at room temperature which is mostly caused by the difference in grain size and lower dislocation density. However there is an increase when comparing these conditions to the *IS* condition which shows that the precipitates created during the processing did indeed have a positive impact on the fatigue properties, which even behaves roughly comparable to an MgZnZr alloy investigated in [39] and [40] not considering any effects introduced by corrosion. However all sample conditions meet the requirement to withstand stresses of up to 25MPa at 5e5 cycles to support bone, thus each condition is viable for usage as implants regarding this property. As samples deformed at elevated temperatures have a lower Young's modulus, closer to that of human bone, they might be best suited concerning stress shielding.

Crack paths of neither *HPT@RT* nor *HPT@RT+HT* conditions are completely straight which is usual for ultra fine grained materials. The behaviour is more visible at the *HPT@RT+HT* condition further hinting toward the brittle nature of the condition. Overall crack paths show a very asymmetrical behaviour when comparing the two faces of the samples, especially when cracking occurred closer to one face than the other; in this case the side closer to the original crack initiation sites shows a more serrated crack path than the other side. Fracture surface images were taken of each condition as well to investigate the crack initiation sited which were all on the edges of the samples and did not occur from impurities or precipitates inside the sample, which is typical behaviour for samples tested at these numbers of cycles to failure. According to expectations the conditions *HPT@RT* and *HPT@RT+HT* showed a smother fracture surface which

is in agreement to the smaller grain size. However *HPT@RT+HT* shows a very brittle behaviour indicated by the numerous microcracks throughout the fracture surface, where all other samples exhibit a ductile behaviour showing fatigue striations along the early stages of the crack path. The *IS* sample shows signs of external force applied to it after cracking, thus destroying the initial surface after fracture.

The use of AE for an in situ measurement of cracking with high time resolution and deformation behaviour concerning dislocations and twinning were only investigated superficially. Yet they show great promise for further investigation in this topic as they allow more precise measurement of cracking and cracking duration. Furthermore if enough information about the AE behaviour of the different sample types is available one could even analyse the sample surface shortly before cracking regarding the creation of intrusions and extrusions on the surface by stopping the fatigue test when certain intensity thresholds are met (compare fig. 50). This however requires many samples to be tested at high numbers of cycles to calibrate the AE set-up correctly which could not be done within the scope of this work.

For further investigation more focus in the AE measurements is encouraged and more SEM images should be recorded to investigate the fracture surfaces. For better sample preparation a sample holder that can be adjusted by a micrometer screw should be designed for a better adjustment of the punching head to allow even more precise and reliable sample preparation, if switching to laser cutting entirely is not feasible. Additional measurement in the regime for 1e6 to 1e7 cycles at lower frequencies could also offer interesting additional data and would eliminate the frequency effect in this important range for biocompatible implants.

References

[1] Günter Gottstein. *Materialwissenschaft und Werkstofftechnik: Physikalische Grundlagen*. Springer Berlin Heidelberg, Berlin, Heidelberg, 4th edition, 2014.

[2] M. Zehetbauer. Effects of non-equilibrium vacancies on strengthening. *Mechanical and corrosion properties. Series A, Key engineering materials*, 97-98:287–306, 1994.

[3] D.R. Askeland, Fulay P.P., and W.J. Wright. The science and engineering of materials. 2010.

[4] Zehetbauer Michael and Zhu Y.T. *Bulk nanostructured materials*. Wiley-VCH ; John Wiley, Weinheim : Chichester, 2009.

[5] Gross Rudolf and Marx Achim. *Festkörperphysik*. De Gruyter, Berlin Boston, 3rd edition, 2018.

[6] Zhang Xie, Tilmann Hickel, Martin Friák, Stefanie Sandlöbes, Biswanath Dutta, and Jörg Neugebauer. Atomic structures of twin boundaries in hexagonal close-packed metallic crystals with particular focus on mg. 3(1):1–7, 2017.

[7] D Hull. *Introduction to dislocations*. Butterworth-Heinemann, Amsterdam, 5th edition, 2011.

[8] R.Z Valiev, Y Estrin, Z Horita, T.G Langdon, Zehetbauer M.J, and Y.T Zhu. Fundamentals of superior properties in bulk nanospd materials. *Materials Research Letters*, 4(1):1–21, 2016.

[9] H. Somekawa and T. Mukai. Hall-petch relation for deformation twinning in solid solution magnesium alloys. *Materials Science and Engineering A*, 561:378–385, 2013.

[10] B. Viguier. Dislocation densities and strain hardening rate in some intermetallic compounds. *Materials Science and Engineering A*, 349(1-2):132–135, 2003.

[11] Pekgüleryüz, Ö Mihriban, K.U. Kainer, and Kaya A. Arslan. *Fundamentals of Magnesium Alloy Metallurgy*. Woodhead Publishing Series in Metals and Surface Engineering. Elsevier Science, 2013.

[12] J.M Hampshire and D Hardie. Hardening of pure magnesium by lattice defects. *Acta Metallurgica*, 22(5):657–663, 1974.

[13] Andrea Ojdanic, Jelena Horky, Bernhard Mingler, Mattia Fanetti, Sandra Gardonio, Matjaz Valant, Bartosz Sulkowski, Erhard Schafler, Dmytro Orlov, and Michael J Zehetbauer. Effects of severe plastic deformation and/or thermal treatment on mechanical properties of biodegradable mg-alloyshigh entropy alloys manufactured by additive manufacturing. *Metals (Basel)*, 10(639), 2020.

[14] M.A Meyers, Mishra A, and D.J Benson. Mechanical properties of nanocrystalline materials. *Progress in Materials Science*, 51(4):427–556, 2006.

[15] R.Z Valiev, Islamgaliev R.K, and I.V Alexandrov. Bulk nanostructured materials from severe plastic deformation. *Progress in Materials Science*, 45(2):103–189, 2000.

[16] W.B Hutchinson and M.R Barnett. Effective values of critical resolved shear stress for slip in polycrystalline magnesium and other hcp metals. *Scripta Materialia*, 63(7):737–740, 2010.

[17] John P Hirth. *Theory of dislocations*. Krieger, Malabar, Fla, 2nd edition, 1982.

[18] Brian S. Mitchell. *An introduction to materials engineering and science for chemical and materials engineers*. John Wiley,, Hoboken, N.J., 2004.

[19] M Pekguleryuz, M Celikin, M Hoseini, Becerra A, and L Mackenzie. Study on edge cracking and texture evolution during 150℃rolling of magnesium alloys: The effects of axial ratio and grain size. *Journal of Alloys and Compounds*, 510(1):15–25, 2012.

[20] Bathias Claude and Pineau André. *Fatigue of materials and structures: Application to Design and Damage*. John Wiley & Sons, Incorporated, Somerset, 2011.

[21] H. Mughrabi. On 'multi-stage' fatigue life diagrams and the relevant life-controlling mechanisms in ultrahigh-cycle fatigue. *Fatigue & Fracture of Engineering Materials & Structures*, 25(8-9):755–764, 2002.

[22] Hael Mughrabi. Damage mechanisms and fatigue lives: From the low to the very high cycle regime. *Procedia Engineering*, 55(C):636–644, 2013.

[23] Mughrabi Hael. On the life-controlling microstructural fatigue mechanisms in ductile metals and alloys in the gigacycle regime. *Fatigue & Fracture of Engineering Materials & Structures*, 22(7):633–641, 1999.

[24] Pedro Peralta and Campbell Laird. 18 - fatigue of metals. In *Physical Metallurgy*, pages 1765–1880. 2014.

[25] E. J. Hearn. *Mechanics of materials 2: The Mechanics of Elastic and Plastic Deformation of Solids and Structural Materials*. Butterworth-Heinemann, Oxford; Boston, 3rd edition, 1997.

[26] Walter D. Pilkey, Pilkey Deborah F., and Bi Zhuming. Notches and grooves. *Strain*, 34:89–166, 2020.

[27] S. Suresh. *Fatigue of materials*. Cambridge University Press, Cambridge; New York, 2nd edition, 1998.

[28] Hael Mughrabi. Specific features and mechanisms of fatigue in the ultrahigh-cycle regime. *International Journal of Fatigue*, 28(11):1501–1508, 2006.

[29] Kakani S.L and Amit Kakani. *Material Science*. New Age International Ltd, New Delhi, 2004.

[30] U Essmann, Gösele U, and H Mughrabi. A model of extrusions and intrusions in fatigued metals I. Point-defect production and the growth of extrusions. *Philosophical magazine. A, Physics odf condensed matter. Defects and mechanical properties*, 44(2):405–426, 1981.

[31] Gu Haicheng, Guo Huifang, Shufen Chang, and Campbell Laird. Orientation dependence of cyclic deformation in high purity titanium single crystals. *Materials Science & Engineering A*, 188(1):23–36, 1994.

[32] Andrea Ojdanic. *Optimization of mechanical properties of biodegradable low-corrosion Mg-alloys by means of severe plastic deformation and thermal treatment*. Wien, 2019.

[33] M Delshadmanesh, G Khatibi, M. Zare Ghomsheh, M Lederer, Zehetbauer M, and H Danninger. Influence of microstructure on fatigue of biocompatible β-phase Ti-45Nb. *Materials Science & Engineering A*, 706:83–94, 2017.

[34] Heather M Tomlinson. An electro-polishing technique for the preparation of metal specimens for transmission electron microscopy. *The Philosophical Magazine: A Journal of Theoretical Experimental and Applied Physics*, 3(32):867–871, 1958.

[35] C.Y Dai, B Zhang, Xu J, and G.P Zhang. On size effects on fatigue properties of metal foils at micrometer scales. *Materials science & engineering. A, Structural materials: properties, microstructure and processing*, 575:217–222, 2013.

[36] Balthasar Fischer. Optical microphone hears ultrasound. *Nature photonics*, 10(6):356, 2016.

[37] Alexei Vinogradov and Kristian Máthis. Acoustic emission as a tool for exploring deformation mechanisms in magnesium and its alloys in situ. *JOM*, 68(12):3057–3062, 2016.

[38] Dong Bian, Weirui Zhou, Yang Liu, Nan Li, Yufeng Zheng, and Zhili Sun. Fatigue behaviors of HP-Mg, Mg–Ca and Mg–Zn–Ca biodegradable metals in air and simulated body fluid. *Acta biomaterialia*, 41:351–360, 2016.

[39] B.J Wang, D.K Xu, J Sun, and En-Hou Han. Effect of grain structure on the stress corrosion cracking (SCC) behavior of an as-extruded Mg-Zn-Zr alloy. *Corrosion science*, 157:347–356, 2019.

[40] D.K Xu and E.H Han. Effect of Yttrium Content on the Ultra-High Cycle Fatigue Behavior of Mg-Zn-Y-Zr Alloys. *Materials science forum*, 816:333–336, 2015.

[41] David Taylor. Fatigue of bone and bones: An analysis based on stressed volume. *Journal of orthopaedic research*, 16(2):163–169, 1998.

[42] Walther Ehalt, Lorenz Böhler, Ernst Purtscher, and E. H. Majer. *Unfallpraxis*. De Gruyter, Berlin, Boston, 2018.

[43] Stefanie Stanzl-Tschegg. Very high cycle fatigue measuring techniques. *International journal of fatigue*, 60:2–17, 2014.

[44] B. Weiss, H. Müllner, R. Stickler, P. Lukas, and L. Kunz. Influence of frequency on fatigue limit and fatigue crack growth behavior of polycrystalline Cu. In *Fracture 84*, pages 1783 – 1790. Pergamon, 1984.

[45] Zijian Li, Xunan Gu, Siquan Lou, and Yufeng Zheng. The development of binary Mg–Ca alloys for use as biodegradable materials within bone. *Biomaterials*, 29(10):1329–1344, 2008.

[46] George E Dieter. *Mechanical metallurgy*. McGraw-Hill series in materials science and engineering. McGraw-Hill, New York, 3rd edition, 2003.

[47] Jason J Williams, Kyle E Yazzie, N Connor Phillips, Nikhilesh Chawla, Xinghui Xiao, Francesco De Carlo, Iyyer Nagaraja, and Maddan Kittur. On the Correlation

Between Fatigue Striation Spacing and Crack Growth Rate: A Three-Dimensional (3-D) X-ray Synchrotron Tomography Study. *Metallurgical and Materials Transactions A*, 42(13):3845–3848, 2011.